Bioactive Materials 39 (2024) 41–58

Contents lists available at ScienceDirect

Bioactive Materials

journal homepage: www.keaipublishing.com/en/journals/bioactive-materials

Targeting micromotion for mimicking natural bone healing by using NIPAM/Nb_2C hydrogel

Qianhao Yang [a,1], Mengqiao Xu [b,1], Haoyu Fang [a,1], Youshui Gao [a], Daoyu Zhu [a], Jing Wang [b,**], Yixuan Chen [a,*]

[a] Department of Orthopedic Surgery, Shanghai Sixth People's Hospital Affiliated to Shanghai Jiao Tong University School of Medicine, Shanghai, 200233, China
[b] Eye Institute and Department of Ophthalmology, Eye and ENT Hospital, Fudan University, Shanghai, 200031, China

ARTICLE INFO

Keywords:
Micromotion
BMSCs
Osteogenesis
Mechanical force
Regenerative medicine

ABSTRACT

Natural fracture healing is most efficient when the fine-tuned mechanical force and proper micromotion are applied. To mimick this micromotion at the fracture gap, a near-infrared-II (NIR–II)–activated hydrogel was fabricated by integrating two-dimensional (2D) monolayer Nb_2C nanosheets into a thermally responsive poly(N-isopropylacrylamide) (NIPAM) hydrogel system. NIR–II–triggered deformation of the NIPAM/Nb_2C hydrogel was designed to generate precise micromotion for co-culturing cells. It was validated that micromotion at 1/300 Hz, triggering a 2.37-fold change in the cell length/diameter ratio, is the most favorable condition for the osteogenic differentiation of bone marrow mesenchymal stem cells (BMSCs). Moreover, mRNA sequencing and verification revealed that micromotion-induced augmentation was mediated by Piezo1 activation. Suppression of Piezo1 interrupts the mechano-sensitivity and abrogates osteogenic differentiation. Calvarial and femoral shaft defect models were established to explore the biocompatibility and osteoinductivity of the Micromotion Biomaterial. A series of research methods, including radiography, micro-CT scanning, and immunohistochemical staining have been performed to evaluate biosafety and osteogenic efficacy. The *in vivo* results revealed that tunable micromotion strengthens the natural fracture healing process through the sequential activation of endochondral ossification, promotion of neovascularization, initiation of mineral deposition, and combinatory acceleration of full-thickness osseous regeneration. This study demonstrated that Micromotion Biomaterials with controllable mechanophysical characteristics could promote the osteogenic differentiation of BMSCs and facilitate full osseous regeneration. The design of NIPAM/Nb_2C hydrogel with highly efficient photothermal conversion, specific features of precisely controlled micromotion, and bionic-mimicking bone-repair capabilities could spark a new era in the field of regenerative medicine.

1. Introduction

As a load-bearing organ, bone tissue constantly receives mechanical stimuli from gravity and the surrounding muscles, which are indispensable for maintaining bone homeostasis and improving matrix and mineral deposition [1,2]. Evolution has energized mammalian skeletal tissues with the capacity for self-repair, in which micromotion and mechanical force play a role [3].

Natural fracture healing is a ubiquitous process in which the bone restores stiffness and mechanical integrity, allowing for sequential revascularization and remodeling. This process includes four overlapping phases: inflammation, soft callus formation, hard callus formation, and remodeling [4]. Briefly, inflammatory cells and circulating bone marrow mesenchymal stem cells (BMSCs) accumulate within the fracture zone, marking the initial stage of bone healing [5]. Depending on the fracture site and local microenvironment, BMSCs can differentiate into either osteoblasts or hypertrophic chondrocytes, initiating intramembranous ossification (IMO) or endochondral ossification (ECO), respectively. The fracture healing process of non-load-bearing bones (e.g., the cranium) is in accordance with the process of

Peer review under responsibility of KeAi Communications Co., Ltd.
* Corresponding author.
** Corresponding author.
E-mail addresses: violaaarom@alumni.sjtu.edu.cn (J. Wang), cyxlp0987@alumni.sjtu.edu.cn (Y. Chen).
[1] These authors contributed equally to this work.

https://doi.org/10.1016/j.bioactmat.2024.05.023
Received 17 January 2024; Received in revised form 9 May 2024; Accepted 10 May 2024

intramembranous ossification, whereas that of weight-bearing bones (e.g., the femur) is in accordance with the process of endochondral ossification. Natural fracture healing of long bones (weight-bearing bones) recapitulates the ECO under axial interfragmentary compression (cyclic axial micromotion at the fracture site) [6,7]. In the absence of inter-fragmentary strain, the bone heals directly following the pattern of IMO, and excessive motion can induce non-union. Finally, the combined promotion of neovascularization and osteoclast activation eventually leads to maturation and remodeling of the primary bone callus [8]. Fine-tuned micromotion is beneficial for successful bone regeneration and endochondral bone development [9,10]. An *in vivo* study demonstrated that mouse digit tip regeneration improved with proper micromotion in damaged areas [11]. However, during bone regeneration the significance of mechanical cues, which are indispensable during cell differentiation, mineral deposition, and matrix maturation, was often neglected [1,2,12]. Glatt et al. reported that interfragmentary micromotion during the early stages (approximately 3 weeks after fracture happens) significantly promoted bone bridging in the defect zone [13,14]. However, excessive micromotion at the fracture ends delays callus formation and maturation, resulting in the failure of internal fixation and an increased probability of nonunion [7,15,16]. The "unstable" biomechanical microenvironment at the fracture site impairs the early local inflammation and the subsequential formation and maturation of bone callus [17].

Inspired by the interpretation of biophysics in natural bone healing, micromotion could be essential for activating the intrinsic capacity for self-repair. Therefore, an elaborate bone graft biomaterial with high biocompatibility, specific features of precisely controlled micromotion, and bionic-mimicking characteristics is of great priority for the reconstruction of bone defect.

The emergence of two-dimensional (2D) nanomaterials has drawn considerable attention over the last few decades. MAX phases, as one of the newly emerging 2D nanomaterials, are generally formulated as $M_{n+1}AX_n$ (in which M stands for a transition metal, A stands for an A group, mostly IIIA and IVA elements, and X stands for C and/or N, with n ranging from 1 to 4) [18–22]. MXenes, which are typically formulated as $M_{n+1}X_nT_x$, are synthesized by extracting the A element from MAX phases [22–27]. In MXenes, "M" resembles an early transition metal atom, "X" represents C or N, and "Tx" stands for surface terminations [23]. The mechanical properties of self-standing MXenes (elastic properties, strength, bending rigidity, interlayer adhesion, and sliding resistance) are determined by several parameters. Specifically, the MXene type (i.e., carbides or nitrides), composition (e.g., mono-/binary/multi-metal), spatial conformation (e.g., mono/few/multi-layer, layer thickness, interlayer spacing, and porosity), preparation method, and modification of different functional groups (e.g., O, OH) synergistically modulate the mechanical properties of MXenes [28,29]. Owing to their outstanding Young's modulus and interlayered structure, MXenes have been extensively utilized as enhancers for promoting the mechanical properties of diverse metals, polymers, and carbon materials [28,30,31]. The unique topological structure and spatial conformation of MXenes endow them with versatile characteristic features, including chemical stability [32], inherent hydrophilicity [33], outstanding electronic conductivity [34], excellent biocompatibility [33,35,36], inherent immunomodulatory features [37], superior photothermal-conversion efficacy [35,36,38], and preeminent antibacterial activity [39–41]. These unique features make MXenes promising candidates for biomedical applications, including tumor ablation and bacterial eradication [26,33,35,38,41–44]. Notably, the superior photothermal-conversion capacity of few- and multi-layer $Ti_3C_2T_x$ MXenes has been utilized in targeted breast cancer photothermal therapy (PTT), which can effectively suppress tumor cell viability within the cancer region [38]. Few- and multi-layer $Ti_3C_2T_x$ MXenes have also been applied to photothermal antibacterial therapy, with prominent bacterial clearance by causing bacterial death linked to the loss of cell integrity [41]. With preeminent photothermal-conversion efficacy and excellent photothermal stability, ultrathin Nb_2C nanosheets exhibited extraordinary tumor eradication efficiency in a 4T1-tumor-bearing mouse model in both NIR-I and NIR-II biowindows [35]. Furthermore, it has been reported that 2D Nb_2C MXenes can not only exert an intensive photothermal effect on osteosarcoma cells for tumor eradication but also facilitate subsequent bone regeneration by inducing osteogenic differentiation and promoting neovascularization [43].

Hydrogels are a family of three-dimensional (3D) polymeric materials with the capability of absorbing and retaining large amounts of water. Owing to their inherent hydrophilicity and high-water content, hydrogels have been widely regarded as an ideal platform for mimicking the hydrated microenvironment for cell growth as well as for biomolecular delivery [45–48]. Recent decades have witnessed the emergence and development of hydrogels in the biomedical field owing to their natural hydrophilicity, excellent biocompatibility, tunable mechanical properties, adjustable degradability, and diverse potential for physicochemical functionalization. Moreover, the crosslinked 3D network and hierarchical porous structure endow hydrogels with satisfactory structural integrity while being tailored into customized sizes and shapes. Diverse hydrogel-based biomaterials have been used in regenerative medicine, including wound patches [49], cartilage repair [50–52], and bone defect regeneration [53,54]. The antitumor activity of hydrogels has also been widely explored. It has been reported that an injectable hydrogel-based bio-niche can augment tumor hypoxia via the oxygen-consumable dimerization process, thus facilitating hypoxia-based chemotherapy [55]. More importantly, increasing growing attention has been paid to the emergence of thermo-responsively controllable shape-changing hydrogels. Poly (N-isopropylacrylamide) (NIPAM) hydrogel, a thermo-responsive deformable hydrogel, exhibits reversible shape-shifting behavior via phase transitions at different temperatures [56]. In addition, the NIPAM hydrogel retained excellent mechanical strength during reversible deformation, which facilitated its application in bone tissue regeneration.

Herein, we report the rational integration of NIR–II–induced photothermal reactivity, highly controllable micromotion, and bone tissue engineering functionalities into a 2D Nb_2C-integrated NIPAM hydrogel scaffold to achieve highly efficient and full-thickness osseous regeneration. The delicate design of the NIPAM/Nb_2C hydrogel scaffold aimed to precisely manipulate the micromotion using external NIR-II in the defect area. We refer to these materials as "***Micromotion Biomaterials***" (Scheme 1). A novel concept of Micromotion Biomaterial was proposed for the acceleration of bone tissue repair in a biomimetic manner. The NIPAM/Nb_2C composite hydrogel can be used as an ideal research platform for generating biomimetic micromotions, thus facilitating the osteogenic differentiation of BMSCs. In this study, we established a mouse calvarial defect model as the non-load-bearing bone defect model and a rat femoral shaft defect model as the weight-bearing bone defect model, which comprehensively demonstrated the impact of micromotion on both intramembranous ossification and endochondral ossification processes. Further understanding of micromotion in cultured BMSCs and the underlying molecular mechanisms would improve the design of ***Micromotion Biomaterials*** and diversify the clinical treatment of massive bone defects.

2. Materials and methods

2.1. Materials

Nb_2AlC powder and tetrapropylammonium hydroxide (TPAOH) were bought through Forsman Scientific Co., Ltd. (Beijing, China). High-purity Nb_2AlC powder (purity level exceeding 99 %) was used in this study. The median particle size (D50) of Nb_2AlC powder was in the range of a few micrometers according to the instruction manual. Aqueous solutions of hydrofluoric acid (HF) and triethanolamine (TEA) were obtained from Sinopharm Reagents Co., Ltd.

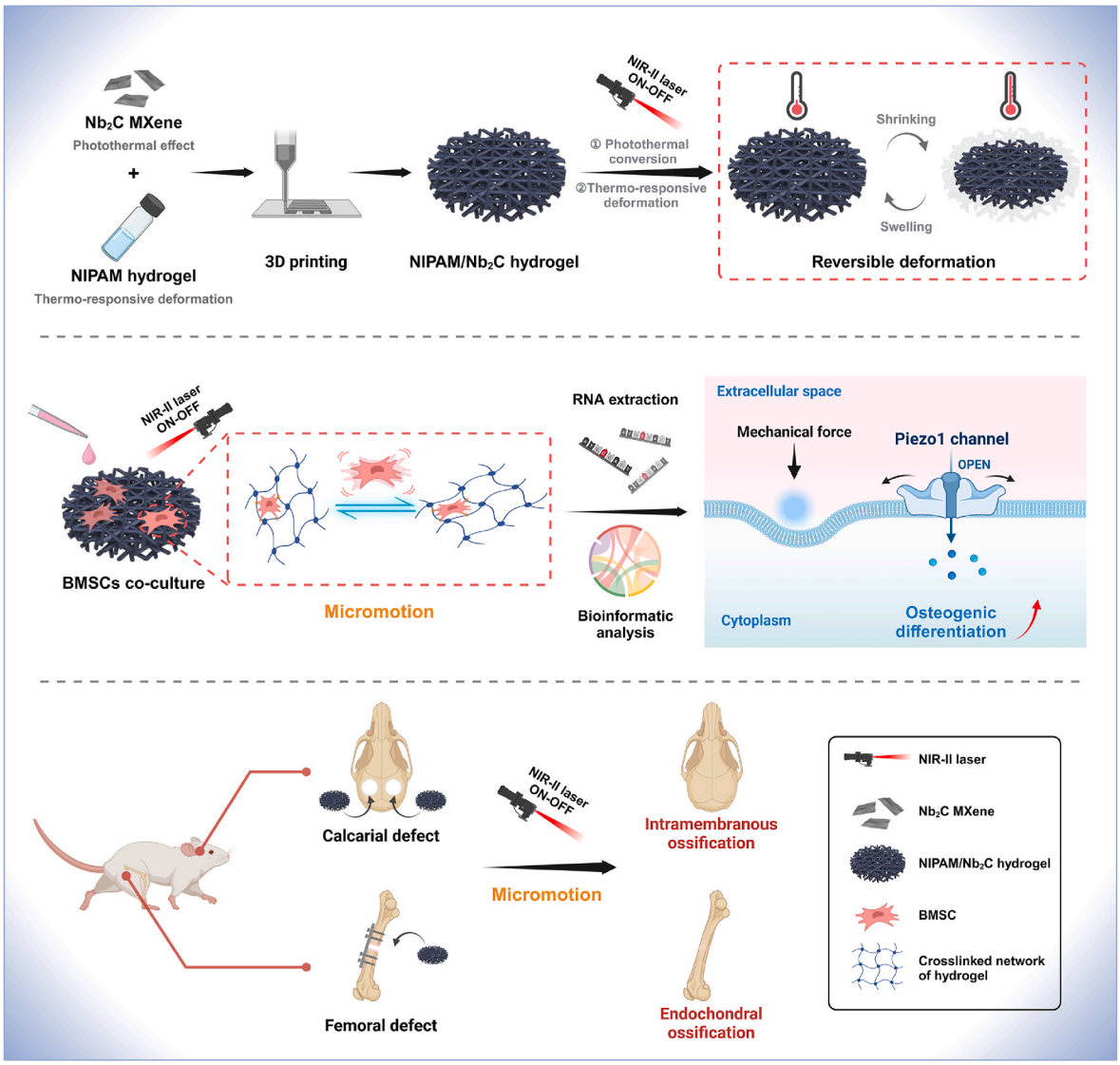

Scheme 1. Schematic representation of systematic correlation of Micromotion Biomaterial, cell fate determination, and bone regeneration. The NIPAM/Nb_2C composite was fabricated by integrating the photothermal effect of Nb_2C MXene nanosheets and the thermo-responsive deformation capability of NIPAM hydrogel. The cyclic "on-off" stimulation of NIR-II irradiation could trigger reversible shrinkage and swelling behavior of the composite, and thus to generate micromotion and facilitate the osteogenic differentiation of BMSCs. High-throughput experiments and bioinformatic analysis revealed that Piezo1 channel was associated with the micromotion-induced osteogenic differentiation of BMSCs. Multiple bone defect models were established to verify the effect of Micromotion Biomaterial on both intramembranous ossification and endochondral ossification.

Cetyltrimethylammonium chloride (CTAC), sodium alginate (SA), 3-mercaptopropyltrimethoxysilane (MPTES), and *t*-butyl nitrite were purchased from Sigma-Aldrich Co., Ltd. (Shanghai, China). Tetraethyl orthosilicate (TEOS) was bought from Lingfeng Chemical Reagents Co., Ltd. (Shanghai, China).

2.2. Synthesis of 2D Nb_2C MXene nanosheets

The 2D ultrathin Nb_2C nanosheets were synthesized through a modified chemical exfoliation procedure, as was demonstrated in previous studies [27,35,43]. Concretely, to obtain mono-layer MXene, 10g multilayer Nb_2AlC powder was dissolved in HF solution (50 %, 60 mL) and then stirred for 48 h at 25 °C to remove the Al layer, which resulted in Nb2C MXene with a "well-stacked" uniform sheet morphology. The precipitate was washed with deionized water and ethanol for 3 times, and then was distributed in the tetrapropylammonium hydroxide (TPAOH) (60 mL, 25 wt%) and stirred for 72 h at 25 °C. Afterwards, the delaminated monolayer Nb_2C nanosheets with typical sheet-like topology were obtained after centrifugation at 3500 rpm for 5 min. This process was repeated for 3 times until predominantly monolayer Nb_2C nanosheets were obtained.

2.3. 3D printing of NIPAM/Nb_2C and SA/Nb_2C scaffolds

The pre-gel aqueous solution containing 2D Nb_2C MXene NSs (0.5, 1.0, and 1.5 mg mL^{-1}), NIPAM (15 % w/v), NMAM (1/10 mass ratio of NIPAM), and LAP (0.1 % v/v). The pre-gel solution of SA/Nb_2C contains SA (2 % w/v) and 2D Nb_2C MXene NSs (1.0 mg mL^{-1}). All solutions were infused into a 3D printing device (LSP01-2A, England) and gathered in a $CaCl_2$ bath (2 % w/v). Then scaffolds were fabricated using an evaporation-induced self-assembly method and a 3D printing technique. The solutions were filled into a polyethylene syringe tube and printed layer-by-layer using a fourth generation 3D Bioplotter™ (Envision^{TEC} GmbH, Germany). Finally, the fibers of scaffolds were crosslinked with UV irradiation (EXFO OmniCure SERIES 1000, 100 W, 365 nm). Scaffolds with different Nb_2C contents were fabricated by using different

Nb_2C-containing pregel solutions (Nb_2C concentrations of 0, 0.5, 1.0, and 1.5 mg mL^{-1}).

2.4. Characterization

For better characterization of the crosslinked network and the hierarchical porous structure of hydrogels in different groups, all hydrogel samples were first immersed in the deionized water for 12 h, and were then freeze-dried at −50 °C by using the Labconco FreeZone Freeze Dryer (Labconco, Kansas City, MO USA). The freeze-dried samples were sputtered with gold using a Cressington 108auto sputter coater (Cressington, Watford, UK) before characterization. The device of scanning electron microscopy (SEM) and elemental mapping images were conducted by using an SU8220 microscope (HITACHI, Japan). Observation of temperature variations were conducted and recorded with infrared thermal imaging instrument (FLIRTM A325SC camera, USA). A multimode laser pump was employed for generating NIR-II laser (Shanghai Connect Fiber Optics Company).

2.5. Photothermal performance and reversible shrinkage and swelling behavior of NIPAM/Nb_2C scaffolds

Surface temperatures of hydrogels were evaluated with infrared thermal imaging instrument. Scaffolds at various initial integrating concentrations (as indicated previously) were exposed to 1064-nm laser at the indicated time intervals to explore the photothermal performance and reversible shrinkage and swelling behavior of the NIPAM/Nb_2C scaffolds. NIPAM/Nb_2C scaffolds were then exposed to indicated laser power densities for observation and measurement of shrinkage and swelling behavior. Finally, the photothermal performance of NIPAM/Nb_2C scaffolds was obtained by applying "on-off" cycles of NIR-II laser stimulation (0.75 W cm^{-2}) and acquiring the shrinkage and swelling behavior patterns.

2.6. In vitro cytotoxicity assay

Human BMSCs were purchased from the cell bank of the Chinese Academy of Sciences (Shanghai, China). In total, 1.5×10^7 BMSCs were cultured in a T25 flask with α-minimum essential medium (Gibco BRL, Grand Island, NY USA). Cells from passages 4 to 6 were utilized in the following experiments. The culture medium was changed daily. Briefly, scaffolds were placed in a 48-well plate and 1.0×10^5 BMSCs were seeded in each well and are allowed 24 h for adhesion. The Cell Counting Kit-8 (CCK-8) (Dojindo Molecular Technologies, Japan) was utilized for measurement of cellular proliferation and toxicity. Live/dead cell staining was conducted to examine the biocompatibility and toxicity of the NIPAM/Nb_2C scaffolds. Dead and live cells showed red and green fluorescence, respectively, as determined using CLSM. For evaluation the deformation of cells by photothermal-reactive micromotion scaffold, the baseline temperature of the incubator is set at 25 °C(room temperature).

2.7. Quantitative reverse transcription polymerase chain reaction (qRT-PCR) analysis

After seeded and co-cultured as described above, cells were harvested mRNA by TRIzol reagent (TransGen Biotech, Beijing, China). qRT-PCR was scheduled by using an ABI HT7900 Sequence Detection System (Applied Biosystems, Australia) as previously described [57]. The primers of COL-I, RUNX2, BMP-2, Piezo1, and OCN were manufactured by BioTNT (Shanghai, China) as follows: COL1: forward: 5′-GAC ATC CCA CCA ATC ACC TG-3′ and reverse: 5′-CGT CAT CGC ACA ACA CCT T-3'; OCN: forward: 5′-AGC CTT TGT GTC CAA GCA-3′ and reverse: 5′-CCA GCC ATT GAT ACA GGT AG-3'; BMP-2: forward: 5′-GGA GGT CGG ATA GTT TCG AT-3′ and reverse: 5′-GCT GGT TGT CGT TCG CTT GA-3'; and RUNX2: forward: 5′-TAA TCT CCG CAG GTC ACT AC-3′ and reverse: 5′-CTG AAG AGG CTG TTT GAT G-3'.

2.8. High-throughput sequencing

Cells were harvested and mRNA were extracted and quantified by using high-throughput sequencing. Total RNA was extracted by using an RNAqueous®-Midi Kit (AM1911, Thermo Fisher Scientific, Waltham, MA USA). High-throughput sequencing was performed in triplicates using an Illumina HiSeq X Ten Second Generation Sequencing Platform (Seq-Health Co., Wuhan, China).

2.9. Alizarin red staining (ARS) and alkaline phosphatase staining (ALP)

After incubation for 48 h, the osteogenic medium was used for osteogenic differentiation, as described previously [58]. Alkaline phosphatase staining was performed on day 14 and calcium deposits were examined by ARS on day 21. Images were captured under an optical microscope.

2.10. Modeling and grouping of calvarial defect

A total of 36 female C57BL/6 mice (20–30 g) were involved in the experiments. Mice were randomly divided into six groups: (1) NIPAM + NIR-II (N = 6), (2) NIPAM/Nb_2C (N = 6), (3) NIPAM/Nb_2C + NIR-II (N = 6), (4) NIPAM + NIR-II OVX (N = 6), (5) NIPAM/Nb_2C OVX (N = 6), and (6) NIPAM/Nb_2C + NIR-II OVX (N = 6). The OVX mice (groups 4, 5, and 6) were ovariectomized 4 weeks before the induction of calvarial defects and implantation of the corresponding scaffold. After 4 weeks, the mice were sacrificed to observe bone healing. The surgical procedures of calvarial defect model are modified from the previous literatures [59–62]. For the surgical procedure, all animals were anesthetized by inhalation of isoflurane. Two 2-mm calvarial defects were manufactured with an electric trephine (Nouvag AG, Goldach, Switzerland), which were later implanted with NIPAM or NIPAM/Nb_2C scaffolds, respectively (Φ 2 mm × 0.5 mm). Antibiotics were administered intramuscularly to each animal postoperatively. No adverse reactions were observed during the experiments. Photothermal therapy with laser irradiation (1064 nm, 0.75 W cm^{-2}, 1 h per day) was performed. The images of temperature change were observed by using an infrared thermal camera (FLIRTM A325SC, USA) during the entire procedure. All mice were sacrificed by over-anesthesia after 4 weeks. The study design of animal experiments was approved by the Animal Research Committee of Shanghai Sixth People's Hospital Affiliated to Shanghai Jiao Tong University School of Medicine (No. 2022-0006).

2.11. Modeling and grouping of femoral shaft defect

Forty-five female Sprague-Dawley rats (200–250 g) were included. For the two-week femoral shaft defect model, 18 rats were divided into three groups: (1) NIPAM + NIR-II (N = 6), (2) NIPAM/Nb_2C (N = 6), and (3) NIPAM/Nb_2C + NIR-II (N = 6). For the 12-week femoral shaft defect model, 36 rats were randomly separated into 4 groups: (1) NIPAM + NIR-II (N = 9), (2) SA/Nb_2C + NIR-II (N = 9) (3) NIPAM/Nb_2C (N = 9), and (4) NIPAM/Nb_2C + NIR-II (N = 9), which were anesthetized by inhalation of isoflurane. The surgical procedures of femoral shaft defect model are modified from the previous literatures [63–66]. One 2-mm defect was created on the femoral shaft using an electric trephine (Nouvag AG, Goldach, Switzerland), which were then filled with NIPAM and NIPAM/Nb_2C, respectively (Φ 2 mm × 1.5 mm). Antibiotics were administered intramuscularly to each animal postoperatively. No adverse reactions were observed during the experiments. Photothermal therapy with laser irradiation (1064 nm, 0.75 W cm^{-2}, 1 h per day) was performed. Rats were sacrificed by over-anesthesia after 3 or 12 weeks, respectively.

2.12. Micro-CT analysis

The bone samples were harvested and then scanned by micro-CT scanner (SkyScan, Kontich, Belgium), which was exhibited at 35 kV/100 μA energy at an 18-μm voxel size. 3D reconstruction images and data statistics including BMD, BV/TV, Tb.Th, and Tb.N were counted and obtained by using the Mimics software and mCT-80 system, as described previously [67–69].

2.13. Histological analysis

Fresh bone samples were decalcification at 25 °C for 1 month and embedded by paraffin after fixation by 4 % paraformaldehyde for 72 h. Next, H&E, Goldner trichrome, TRAP, safranin O-Fast green, and immunohistochemical staining were prepared with 5-μm sections. The antibodies for OCN, RUNX2, MMP13, COL-10, Piezo1, and CD31 were bought from Abcam (Cambridge, MA). Those images were performed with LEICA DM 4000 microscope and SP8 confocal microscope (Leica, Solms, Germany). For hard tissue sections, samples were embedded and processed according to a previous standard [70], and Van Gieson staining was performed on the hard tissue slices.

2.14. Statistical analysis

All data are presented as means ± standard deviations. Statistical were executed utilizing Student's two-sided *t*-test, with *P < 0.05 (indicating statistical significance), **P < 0.01 (indicating moderate significance), and ***P < 0.001 (indicating high significance).

3. Results

3.1. Synthesis and characterization of NIPAM/Nb_2C scaffolds

Generally, near-infrared-ray (NIR)–II–responsive scaffolds are fabricated by mixing Nb_2C nanosheets (NSs) into a thermally responsive poly(N-isopropylacrylamide) (NIPAM) hydrogel by using a facile solution-soaking approach, endowing NIPAM/Nb_2C with a specifically controllable deformation ability by NIR–II–induced photothermal ablation. Specifically, NIPAM/Nb_2C was functionalized with Nb_2C NSs at different concentrations (0.5, 1.0, and 1.5 mg mL^{-1}) to achieve different loading amounts.

The digital images (Fig. 1a) indicated that the NIPAM/Nb_2C scaffolds were manufactured by using a 3D additive technique. The microstructure of the NIPAM scaffolds with Nb_2C MXene provided a unique microenvironment and a controllable deformation capacity suitable for osteogenesis and osteointegration. The NIPAM/Nb_2C scaffolds exhibited a gradually deepening black color, with an incremental loading concentration of Nb_2C. Scanning electron microscopy (SEM) images (Fig. 1b–d) depicted Nb_2C spreading on the rough surface of the NIPAM fiber. Element-mapping analysis of the scaffold cross-section demonstrated homogeneous elemental distributions, where N and H tended to gather on the interior surface. Nb and C were enriched in the fractured cross-section, which could be attributed to the conglutination of Nb_2C (Fig. 1e).

3.2. Photothermal responsive performance and deformability of NIPAM/Nb_2C scaffolds

The volume capacity and temperature of NIPAM and NIPAM/Nb_2C scaffolds were monitored under irradiation with a 1064-nm laser at 1.0 W cm^{-2} for different time intervals (Fig. 2a and b). Under the same irradiation condition, the NIPAM/Nb_2C scaffolds temperature increased from 22.7 to 44.2 °C in comparison with the minor change in pure NIPAM scaffolds. NIPAM exhibited reversible volume changes at different temperatures, indicating that the hydrogel swelled or shrunk when the temperature was below or above the LCST, respectively. In our previous research, we adjusted poly (NIPAM) to around 40 °C by copolymerizing NIPAM and N-methylol acrylamide (NMAM) at a volume ratio (VR) of 90 %. The sensitivity of the reversible shrinkage and swelling behaviors of the NIPAM/Nb_2C scaffolds to temperature fluctuations was pronounced and contingent on the power density of laser exposure. We ascertained the biocompatibility of both the NIPAM and NIPAM/Nb_2C variations through live-dead cell staining and the Cell Counting Kit-8 (CCK-8) assay, confirming their excellent biocompatibility (Fig. 2c and g). The photothermal heating pattern of the NIPAM/Nb_2C scaffold aligned with that in Fig. 2a, attaining a peak at 44 °C. Moreover, the photothermal heating effect remained robust even after repeated stimulation with NIR-II irradiation, signifying the persistent photothermal efficiency of the NIPAM/Nb_2C scaffolds (Fig. 2e). Fig. 2e displays the modulated reversible shrinkage and swelling behavior of the NIPAM/Nb_2C scaffolds under NIR-II irradiation. When the temperature of the NIPAM/Nb_2C scaffolds peaked at 38 °C (after 350 s of NIR-II irradiation, Fig. 2d and f), they contracted approximately 10 % in volume, subsequently regained 100 % volume upon natural cooling to room temperature (25 °C). In aggregate, these findings validate the replicable and controllable NIR–II–responsive behavior of NIPAM/Nb_2C scaffolds.

3.3. Micromotion biomaterial triggered the elongation of BMSCs and promoted osteogenic differentiation

To understand the impact of cyclic stretching of NIPAM/Nb_2C scaffolds on the behavior of BMSCs, different frequencies of NIR-II irradiation were used in our study. The aspect ratio (AR, the ratio of cell length/diameter) of BMSCs was used for the quantitative evaluation of cell stretching. Under the case of 24-h stimulation, 1/300 Hz proved to be the most effective frequency for cell stretching on the NIPAM/Nb_2C scaffolds. Moreover, only NIPAM/Nb_2C under NIR-II irradiation exhibited excellent cell stretching ability (Fig. 3a–c). To avoid the osteogenic effects of elevated temperatures [71], we fabricated a sodium alginate (SA)/Nb_2C scaffold, which could be heated but did not deform upon parallel NIR-II irradiation. Fig. 3d and e shows the measurement and quantification of the AR of BMSCs co-cultured with the NIPAM/Nb_2C scaffold. The intricately designed structure of the composite scaffold, which had exceptional biocompatibility, established an ideal microenvironment for the proliferation, differentiation, and adhesion of BMSCs. Moreover, high cell attachment performance may facilitate osseointegration *in vivo*. We observed that the co-cultured BMSCs demonstrated significant elongation after 24 h of 1/300 Hz NIR-II light treatment (Fig. 3f). No significant cell elongation was observed in the SA/Nb_2C or SA/Nb_2C + NIR-II groups. Osteogenic differentiation of BMSCs was confirmed by polymerase chain reaction (PCR) analysis of the expression of various osteogenic genes, including collagen (*COL-1*), osteocalcin (*OCN*), bone morphogenetic protein 2 (*BMP-2*), and runt-related transcription factor 2 (*RUNX2*). These osteogenic genes were detected, and their expression levels were compared among the different groups. (Fig. 3g). The expression of all osteogenic genes was significantly enhanced in the NIPAM/Nb_2C + NIR-II group. Furthermore, Alizarin red staining (ARS) was performed to assess the mineralization and calcium deposition of BMSCs in different groups. Notably, the NIPAM/Nb_2C + NIR-II group exhibited a significant augmentation in calcium nodules compared with the other groups following 21 days of osteogenic induction. (Fig. 3h). Furthermore, staining for alkaline phosphatase (ALP), the hallmark enzyme of mature osteoblasts, was conducted to verify the osteogenic ability of the NIPAM/Nb_2C group under NIR-II irradiation (Fig. 3i and k). These data suggest that micromotion induces cell elongation and enhances osteogenic differentiation of BMSCs.

3.4. Cyclic stretching at 1/300 Hz proved to be the most efficient in promoting osteogenic differentiation of BMSCs

We discovered that the NIPAM/Nb_2C scaffolds generated a certain

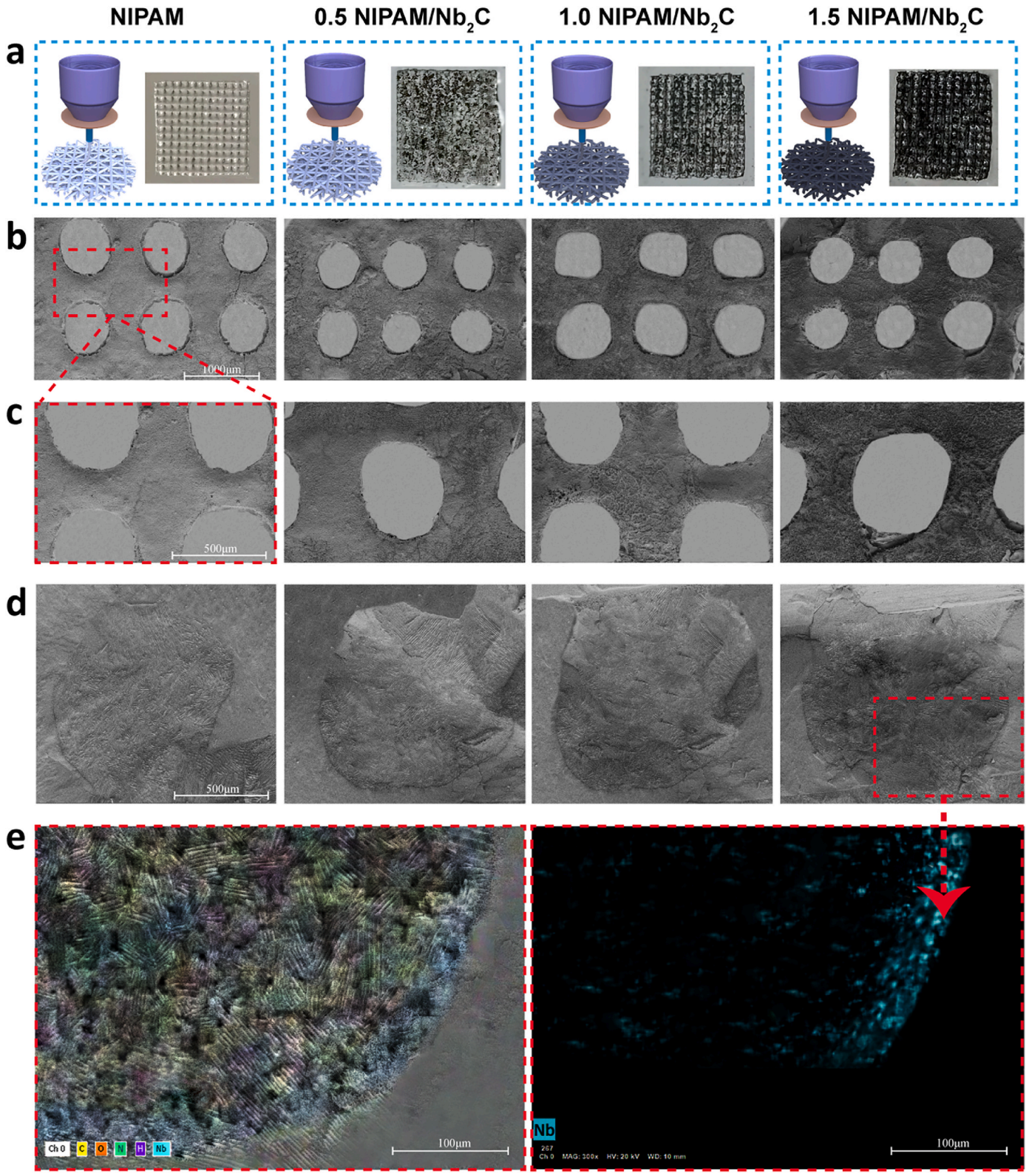

Fig. 1. Synthesis and characterization of NIPAM/Nb_2C scaffolds. a) Digital photographs of pure poly(N-isopropylacrylamide) (NIPAM) and NIPAM/Nb_2C variants, including 0.5, 1.0, and 1.5 NIPAM/Nb_2C.b-d) Corresponding SEM images of pure NIPAM and NIPAM/Nb_2C variants. From top to bottom, scale bar represents 1000, 500, and 500 μm, respectively. Each row of images shares the same scale bar. e) Fracture structure and element mappings of 1.5 NIPAM/Nb_2C. Scale bar: 100 μm.

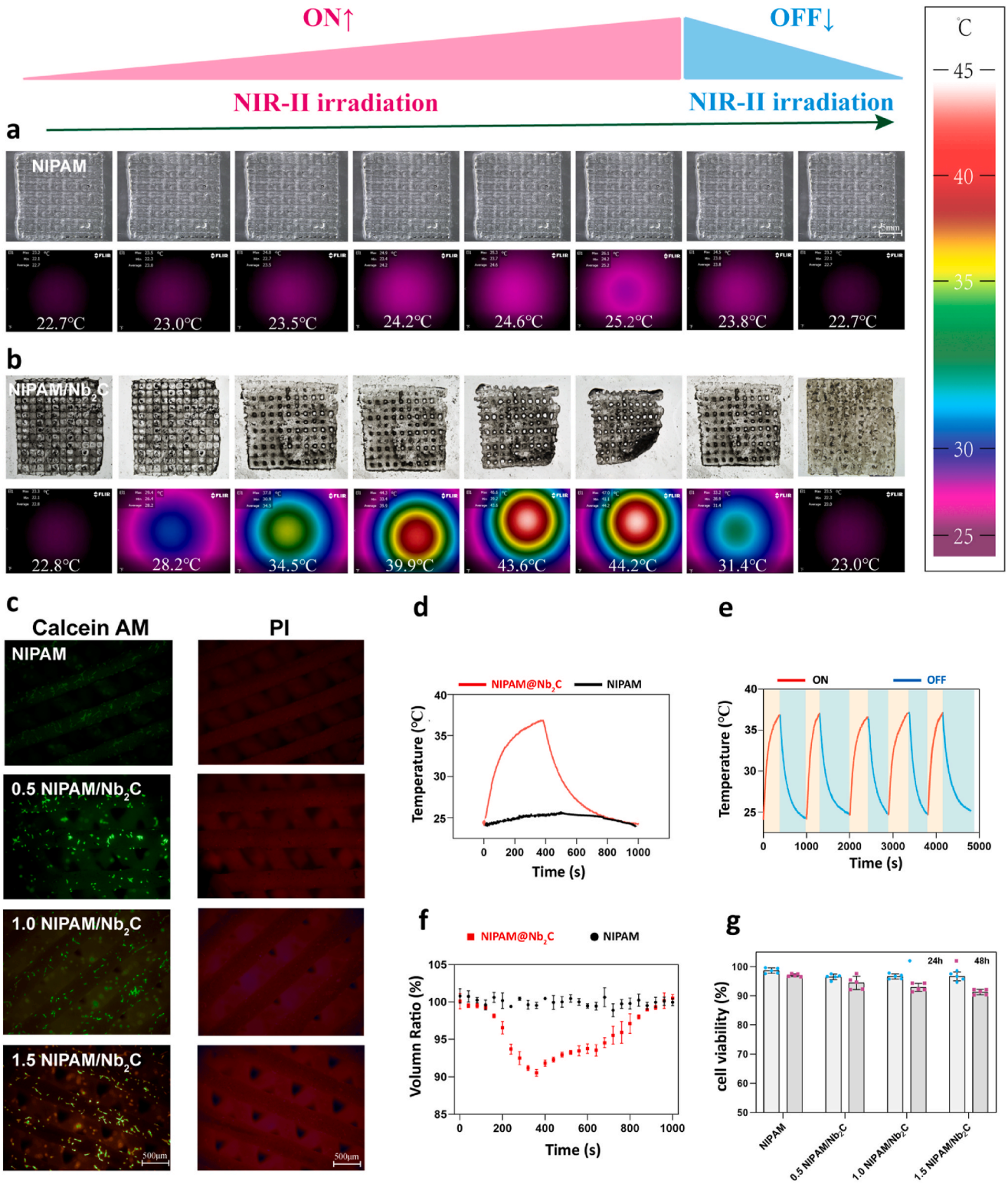

Fig. 2. Photothermal responsive performance and deformability of NIPAM/Nb_2C scaffolds. a) Real-time photograph and thermal images of NIPAM scaffolds (under NIR-II laser irradiation at 1.0 W cm^{-2} for different time intervals). Scale bar: 5 mm. b) Real-time photograph and thermal images of NIPAM/Nb_2C scaffolds (under NIR-II laser irradiation at 1.0 W cm^{-2} for different time intervals). Scale bar: 5 mm. c) CLSM images of BMSCs cells stained with calcein AM (live cells, green fluorescence) and PI (dead cells, red fluorescence) on NIPAM and NIPAM/Nb_2C variants as indicated in the Figure. Scale bar: 500 μm. d) Photothermal heating curves of NIPAM and NIPAM/Nb_2C scaffolds when exposed to NIR-II laser irradiation at 0.75 W cm^{-2} for 400 s. e) Temperature variation over five ON (red line)/OFF (blue line) cycles of NIR-II irradiation (0.75 W cm^{-2}, 1000 s for a cycle). f) The cyclic shrinkage of volume ratio (VR) of NIPAM and NIPAM/Nb_2C scaffolds when exposed to NIR-II laser irradiation at 0.75 W cm^{-2} for 400 s (ON) and followed by naturally cooling to room temperature without irradiation for 600 s (OFF). N = 5. g) Relative cell viability of BMSCs cells treated with NIPAM and NIPAM/Nb_2C variants at 24 and 48 h using CCK-8. N = 5, *p < 0.05, **p < 0.01, and ***p < 0.001.

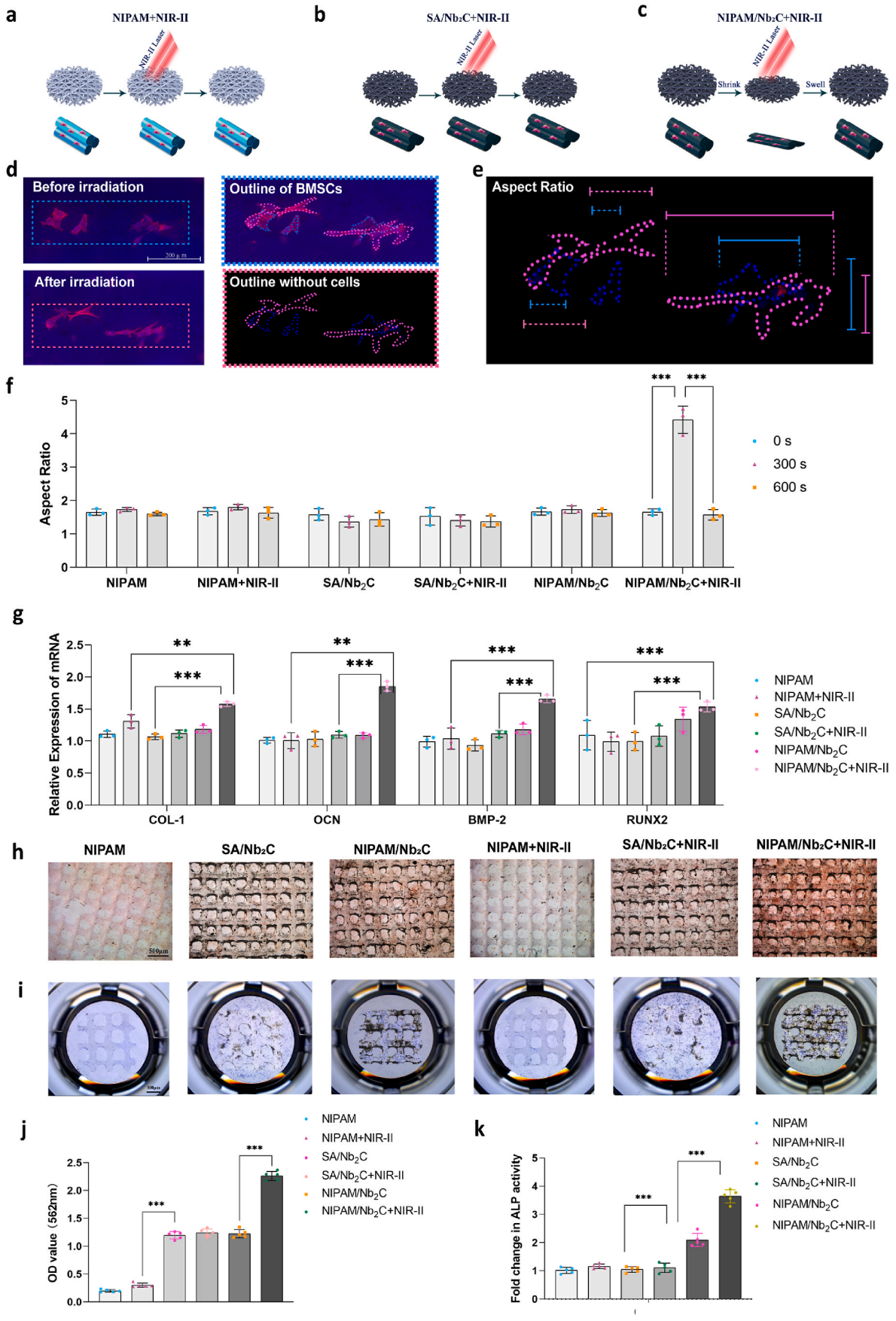

(caption on next page)

Fig. 3. Micromotion biomaterial triggered the elongation of BMSCs and promoted osteogenic differentiation. a-c) The schematic diagram of the elongation dependent on different scaffold. d) The dynamic changes of co-cultured BMSCs in the whole stretching cycle at 1/300 Hz on NIPAM/Nb_2C after 24 h. Scale bar is 200 μm. e) The diagrammatic sketch of the Aspect Ratio (AR) measurement. Blue and pink line represent the length and width of BMSCs and which after irradiation respectively after 24 h. f) The AR of BMSCs at 0 s, 300 s, and 600 s on different scaffolds (as indicated) under 1/300 Hz of cyclic stretching after 24 h of co-culture. N = 3, *p < 0.05, **p < 0.01, and ***p < 0.001. g) Osteogenic gene expression (COL-1, OCN, BMP-2, and RUNX2) of BMSCs on day 7 in different groups. N = 3, *p < 0.05, **p < 0.01, and ***p < 0.001. h) ARS after incubation for 21 days in different groups. Scale bar is 500 μm. i) ALP staining after incubation for 14 days in different groups. Scale bar is 500 μm. j, k) Quantitative statistics of ARS staining and ALP staining. N = 5, *p < 0.05, **p < 0.01, and ***p < 0.001.

frequency of micromotion that triggered the elongation of BMSCs and promoted their osteogenic differentiation. We do not know which frequency range is most beneficial. Next, we investigated the role of decisive mechanical factors, including morphological changes in the scaffold (VR) and different frequencies of cycling stretch, on the morphological changes (AR) and osteogenic differentiation of BMSCs (OD value of ARS) (Fig. 4a and b). Fig. 4b and e shows CLSM images of BMSCs adhering to the NIPAM/Nb_2C scaffold with different frequencies of NIR-II light stimulation. As shown in Fig. 4l, ARS and ALP assays were performed after incubation for 21 and 14 days, respectively, under different mechanical conditions. The results indicated that the NIPAM/Nb_2C scaffold under 1/300 Hz of NIR-II generated an excellent stretch-shrink pattern (VR alteration of 8.5 %) and a superior osteogenic effect. Simultaneously, we observed an almost double increase in the OD value of ARS and the most prominent osteogenic differentiation of BMSCs (Fig. 4i, **l**).

Furthermore, for summarization and quantification, equation fitting was performed, which illustrated the general trend of the frequency with AR and osteogenic ability, indicating a peak at 1/300 Hz (Fig. 4f and h). Fig. 4g depicts the equation fitting and line plots of the relationship between frequency and VR, indicating a maximum VR alteration (9.7 %) at 1/350 Hz on the NIPAM/Nb_2C scaffold. In these equations, a and b are constant parameters. Fig. 4i shows the line plots of the relationship between the maximum VR and the osteogenic ability over the entire cycle, indicating the maximum OD value of ARS with a VR alteration of 8.5 % on the NIPAM/Nb_2C scaffold. In Fig. 4j and k, to provide a more intuitive description of the above four figures, we simplified the data and selected the micromotion frequencies at 1/150, 1/300, 1/450, 1/600, and 1/750 Hz as independent variables, and the VR of the biomaterial and/or the OD value of the ARS as dependent variables. We found that a micromotion frequency of 1/300 Hz could cause a maximum change in the OD value of up to more than two times with a VR alteration of 8.5 % (Fig. 4j and k). It is noticed that a micromotion frequency of 1/350Hz induced a maximum VR alteration of 9.7 % and a maximum AR change, whereas a micromotion frequency of 1/300 Hz resulted in the highest OD value with a VR alteration of 8.5 %. This unparalleled data might be ascribed to cellular tolerance to mechanical forces. Combining these data, we concluded that micromotion at 1/300 Hz was the most efficient in promoting the osteogenic differentiation of BMSCs.

3.5. *Micromotion Biomaterial enhanced bone regeneration in femoral shaft defect through the activation of endochondral ossification*

Multiple animal models were used to evaluate the osteoinduction activity of NIPAM/Nb_2C scaffolds *in vivo*. First, a rat femoral shaft defect model was established (Fig. 5b). The animals were sacrificed 12 weeks after surgery to investigate bone healing following the micromotion stimulus (Fig. 5a). After each treatment, which encompassed the surgical implantation of different composite scaffolds and NIR-II irradiation, 3D modeling of the micro-computed tomography (micro-CT) data was reconstructed. Subsequent analyses were performed to delve deeper into these results (Fig. 5d). Radiography revealed more prominent new bone formation around the defect area in the NIPAM/Nb_2C + NIR-II group (Fig. 5c). Micromotion stimulus significantly increased the volume of the bone callus around the fracture gap. Moreover, the 3D reconstruction of the harvested femur revealed distinctly calcified tissue surrounding the defect with NIPAM/Nb_2C under NIR-II irradiation (Fig. 5d). The 3D models were classified as the newly regenerated bone, osteoid, and compact bone using yellow, green, and blue colors, respectively. The steel plates in each group were labeled with pink color (Fig. 5e and f). For the quantitative assessment of regenerated bone, essential parameters including bone mineral density (BMD), bone volume/tissue volume (BV/TV), trabecular thickness (Tb.Th), and trabecular number (Tb.N) were employed. These parameters were utilized to perform a thorough quantitative analysis of the newly formed bone tissue (Fig. 5g). The NIPAM/Nb_2C + NIR-II group exhibited a significantly elevated BV/TV ratio, indicating a higher percentage of newly formed bone tissue within the defect spaces. These results indicated that new bone formation was significantly enhanced in the NIPAM/Nb_2C + NIR-II group. Collectively, these data revealed that appropriate micromotion enhanced bone healing in the femoral shaft defect model.

Van Gieson staining of the undecalcified bone slices revealed robust healing of the bone fracture, with minimal remaining bone calluses observed in the NIPAM/Nb_2C + NIR-II group (Fig. 5i). The other groups exhibited less new bone formation around the fracture sites, instead of displaying a continuous bony bridge connecting both sides. The results of hematoxylin and eosin (H&E) and Goldner staining showed similar trends (Fig. 5j and k). As shown in Fig. 5i and m, the positive staining for OCN and CD31 increased in the NIPAM/Nb_2C + NIR-II group compared to that in the other groups. Quantification data indicated that osteogenic activity and neovascularization in the defect area of the weight-bearing bone were more prominent under the micromotion stimulus (Fig. 5n).

To observe dynamic bone healing, a parallel rat femoral shaft defect model was established, and the animals were sacrificed 3 weeks after surgery to investigate endochondral ossification (ECO) upon micromotion stimulus. Radiography and micro-CT were performed 3 weeks postoperatively. We found that the rats in the NIPAM/Nb_2C + NIR-II group had a significantly increased volume of soft callus (Figs. S1 and S2). This was confirmed by immunohistochemical staining of MMP-13. MMP-13 is a unique marker of hypertrophic chondrocyte differentiation. The results showed more MMP-$13^{(+)}$ cells and $CD31^{(+)}$ vasculature in the NIPAM/Nb_2C + NIR-II group than in the other two groups (Figs. S3 and S4). This indicated the tunable micromotion at the fracture site activated the function and transdifferentiation of hypertrophic chondrocytes, which in turn accelerated the secretion of vascular endothelial growth factor (VEGF) and neovascularization [72]. Fewer bone calluses were detected in the NIPAM + NIR-II group. This is consistent with the consensus that a low strain at the fracture gap with stable fixation leads to no bone callus formation or non-union. These findings indicate that the promotion of bone healing by micromotion stimuli could be ascribed to the enhanced function and transdifferentiation of hypertrophic chondrocytes.

3.6. *Micromotion Biomaterial increased bone healing and angiogenesis in calvarial defect model*

To examine the impact of micromotion on the healing process of non-weight-bearing bones, a mouse model of calvarial defects was established. This model was utilized to investigate the *in vivo* osteogenic and angiogenic capabilities of the NIPAM/Nb_2C scaffolds, as well as their influence on bone regeneration. (Fig. 6a).

Four weeks after surgery, all mice were sacrificed and calvarial bone samples were harvested. The micro-CT data indicated more prominent new bone formation around the defect area in the NIPAM/Nb_2C + NIR-II group (Fig. 6b and c). Quantitative fundamental parameters, including BMD, Tb.Th, BV/TV, and Tb.N, were markedly higher in the NIPAM/

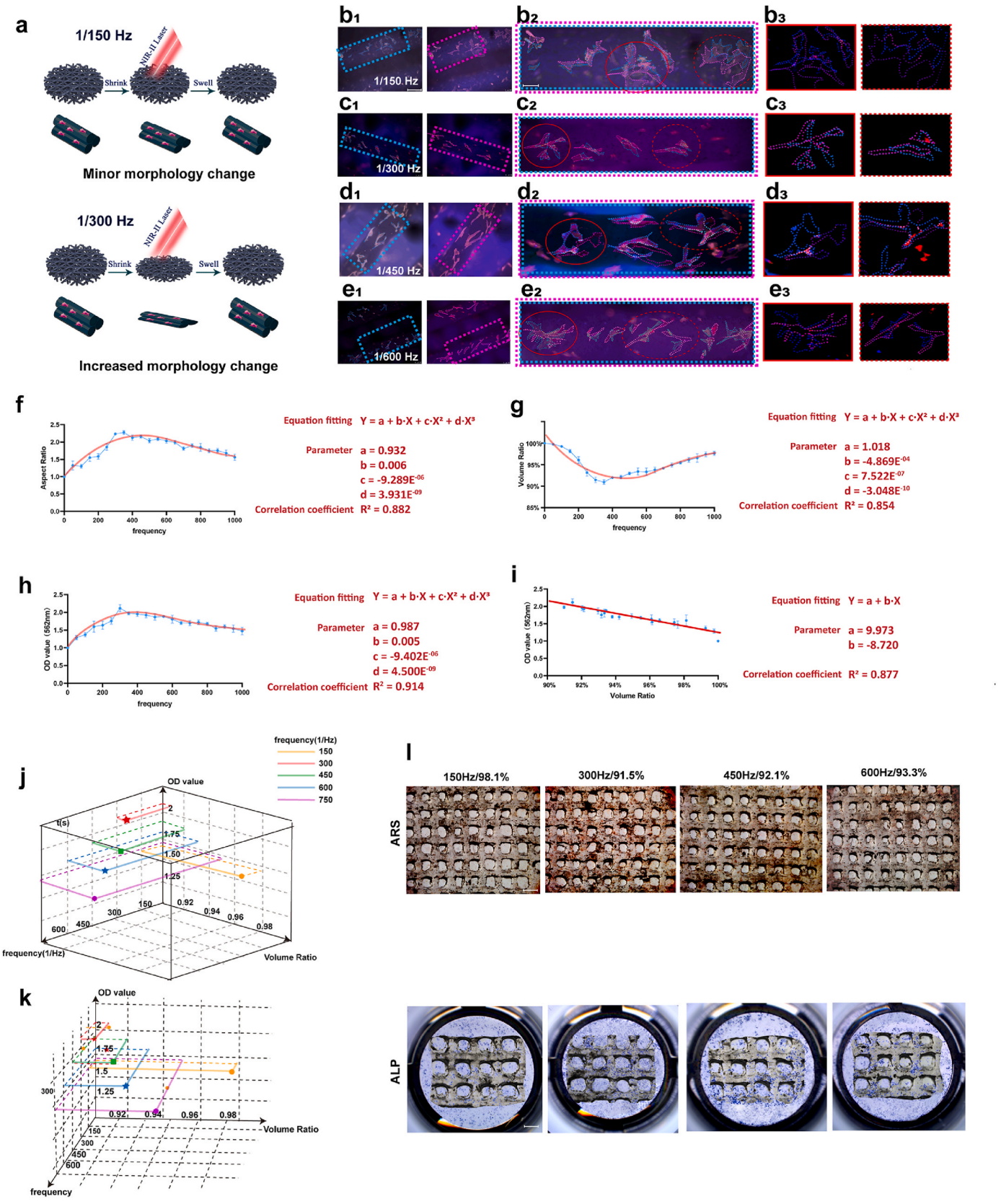

(caption on next page)

Fig. 4. Cyclic stretching at 1/300 Hz proved to be the most efficient in promoting osteogenic differentiation of BMSCs. a) The schematic diagram of the elongation of co-cultured BMSCs dependent on the frequency of stretching. b-e) CLSM images of BMSCs adhering on the NIPAM/Nb_2C scaffold with different frequency of NIR-II light stimulation. Cells were stained with DAPI (cell nuclei, blue fluorescence), rhodamine phalloidin (cytoskeleton, red fluorescence). The left row and blue dotted line in b1–e1 represent the outline of co-cultured BMSCs (at 0 s), while the pink dotted line (right row) in b1–e1 represents the BMSCs under NIR-II irradiation (at 150 s, 300 s, 450 s, or 600 s). Scale bar is 200 μm. b2–e2 the merge images demonstrate dynamic changes of BMSCs under different conditions Scale bar is 50 μm. b3–e3 indicate the enlarged parts of the red circles in b2–e2. f) The line plots of the relationship between frequency and AR of BMSCs in the whole cycle demonstrating maximum elongation at 1/350 Hz on NIPAM/Nb_2C (AR of 2.5), observed at 24 h (N = 10 for each microscopic field, tests were replicated for three times). g) The line plots of the relationship between frequency and volume ratio showed maximum VR alteration at 1/350 Hz on NIPAM/Nb_2C (VR alteration of 9.7 %), observed at 24 h. The line plots of the relationship between frequency, AR, and VR in the whole cycle demonstrating maximum elongation at 1/350 Hz on NIPAM/Nb_2C (AR of 2.5) (N = 3). h) The line plots of the relationship between frequency and osteogenic ability in the whole cycle demonstrating maximum OD value of ARS at 1/300 Hz on NIPAM/Nb_2C (N = 3). i) The line plots of the relationship between VR and osteogenic ability in the whole cycle demonstrating maximum OD value of ARS with VR alteration of 8.5 % on NIPAM/Nb_2C (N = 3). j-k) The three-dimensional coordinate of osteogenic ability with the variation of frequency and volume ratio. Different line colors indicate different frequencies (1/Hz). l) ARS and ALP staining after osteogenic induction in different groups with the variation of frequency and volume ratio. Scale bar is 500 μm.

Nb_2C + NIR-II group (Fig. 6j). Micromotion stimulus significantly promoted new bone formation in the defective areas of the NIPAM/Nb_2C + NIR-II group. Four weeks postoperatively, samples from each group were subjected to hematoxylin and eosin (H&E) and Goldner staining. In each group, the scaffolds were completely degraded, with no discernible inflammatory response or signs of necrosis (Fig. 6f and g). The NIPAM/Nb_2C + NIR-II group exhibited substantial formation of new bone, whereas less bone formation was observed in the NIPAM/Nb_2C and NIPAM + NIR-II groups. As shown in Fig. 6h, significantly more positive staining for OCN was observed in the new bone tissue of the NIPAM/Nb_2C + NIR-II group, indicating accelerated osteogenic activity upon micromotion stimulation. Collectively, these data revealed that appropriate micromotion enhanced bone healing in the calvarial bone defect model. 3D reconstruction of vascular perfusion was performed to visualize neovascularization in bone defects. We observed a more prominent neovascularization in the defect area in the NIPAM/Nb_2C + NIR-II group (Fig. 6d). To verify this, immunohistochemical analysis of CD31 was performed on bone samples. The results confirmed that micromotion enhanced angiogenesis in new bone tissues (Fig. 6i, Fig. S6b). However, our data showed no significant differences in nerve formation in defective areas (Figs. S5 and S6a).

To assess the impact of micromotion on bone healing in an osteopenia model characterized by compromised bone structure, diminished bone mass, and heightened fracture susceptibility, we constructed a calvarial defect in an ovariectomized (OVX) model. All animals were ovariectomized 4 weeks before calvarial defect surgery and implantation of the corresponding scaffold. After another 4 weeks, all animals were sacrificed to observe bone healing (Fig. 6a). The micro-CT data demonstrated a marked increase in new bone formation in the NIPAM/Nb_2C + NIR-II group compared to the other two groups at 4 weeks (Fig. 6b). Further analysis using H&E and Goldner staining showed greater bone formation and collagen deposition in the NIPAM/Nb_2C + NIR-II group than in the other two groups. Histological evaluations indicated that the bone-healing efficacy of NIPAM/Nb_2C + NIR-II was notably superior to that of the other two groups. This finding was consistent with the micro-CT results (Fig. 6j). The measurement and analysis of CD31 and OCN expression demonstrated that the NIPAM/Nb_2C + NIR-II and NIPAM/Nb_2C groups had better angiogenic and osteogenic potentials (Fig. 6h and i). In addition, the 3D reconstruction of vascular perfusion revealed more prominent neovascularization in the defect area of the NIPAM/Nb_2C + NIR-II group, which was in consistency with the results of immunohistochemical staining. The outcomes of *in vivo* data, including micro-CT scans, H&E staining, and immunohistochemical staining, collectively verified the therapeutic effect of NIPAM/Nb_2C scaffolds on calvarial defects.

3.7. Micromotion-induced osteogenic differentiation of BMSCs is associated with Piezo1 protein

To elucidate the underlying molecular mechanisms, mRNA sequencing was performed on BMSCs (NIPAM + NIR-II, NIPAM/Nb_2C, and NIPAM/Nb_2C + NIR-II groups; $N = 3$). The top 50 differentially expressed genes in the mRNA sequencing results (downregulation: fold change <0.5, $^*p < 0.05$; upregulation: fold change >1.5, $^*p < 0.05$) in the NIPAM/Nb_2C + NIR-II group showed significantly different gene expression compared to those in the other groups, based on the heatmap and volcano map (Fig. 7a and b). Using gene set enrichment analysis (GSEA), we identified osteoblast differentiation and mechanoreceptor pathways as two critical biological processes in BMSCs upon micromotion stimulation (Fig. 7c and f). Gene Ontology (GO) pathway analysis of the mRNA sequencing results revealed that the physiological processes of the extracellular matrix and cell adhesion played critical roles (Fig. 7d and e), which was also verified by the GO enrichment cluster and doughnuts (Fig. 7g and h). For further investigation, we conducted STRING analysis of differential genes (https://cn.string-db.org/) and found that Piezo1 played an important role in the entire process (Fig. 7i). In the living body, cells constantly receive and respond to microenvironmental mechanical cues by deforming themselves [73,74], mainly through a special membrane receptor called Piezo [75,76]. The Piezo1 channel is the predominant member of the Piezo family [77], which is capable of sensing mechanical cues and converting them into biological signals [78]. Piezo1 channel activation is associated with the osteogenic differentiation of BMSCs. In our study, we found that Piezo1 expression increased in the NIPAM/Nb_2C + NIR-II group, which is in line with the ARS results. Downregulation of Piezo1 in co-cultured BMSCs significantly decreased osteogenic differentiation. These data indicate that Piezo1 plays a critical role in the micromotion-mediated osteogenic differentiation of BMSCs. Using a selective activator (Yoda1) or inhibitor (GsMTx4) of Piezo1, we silenced and activated Piezo1. The results showed that Yoda1 significantly promoted the osteogenic capacity of BMSCs (ARS staining) and expression of osteogenic genes, including *COL-I*, *RUNX2*, *BMP-2*, and *OCN* (Fig. 7j and k) in BMSCs. Inhibition of Piezo1 prevented the micromotion-induced upregulation of osteogenesis-related genes and calcium deposition. These results agree with the *in vivo* data that Piezo1 positive staining was upregulated upon micromotion stimulation (Fig. 7l–m). These findings suggest a correlation between micromotion-induced osteogenic differentiation of BMSCs and Piezo1 expression.

4. Discussion

The skeletal system requires continuous mechanical stimulation to promote bone development and self-repair [6,79,80]. To date, researchers have primarily focused on improving the biological and chemical characteristics of bone substitutes [67,68,81–83]. However, studies on the biophysics and cell biology of bone healing indicate that micromotion is essential for the activation of the intrinsic capacity for self-repair. Inspired by this biomimetic principle, we fabricated a NIPAM/Nb_2C hydrogel that integrated controllable micromotion into a highly biocompatible scaffold, which proved to be an applicable method for bone regeneration.

First, we determined the most favorable mechanical environmental

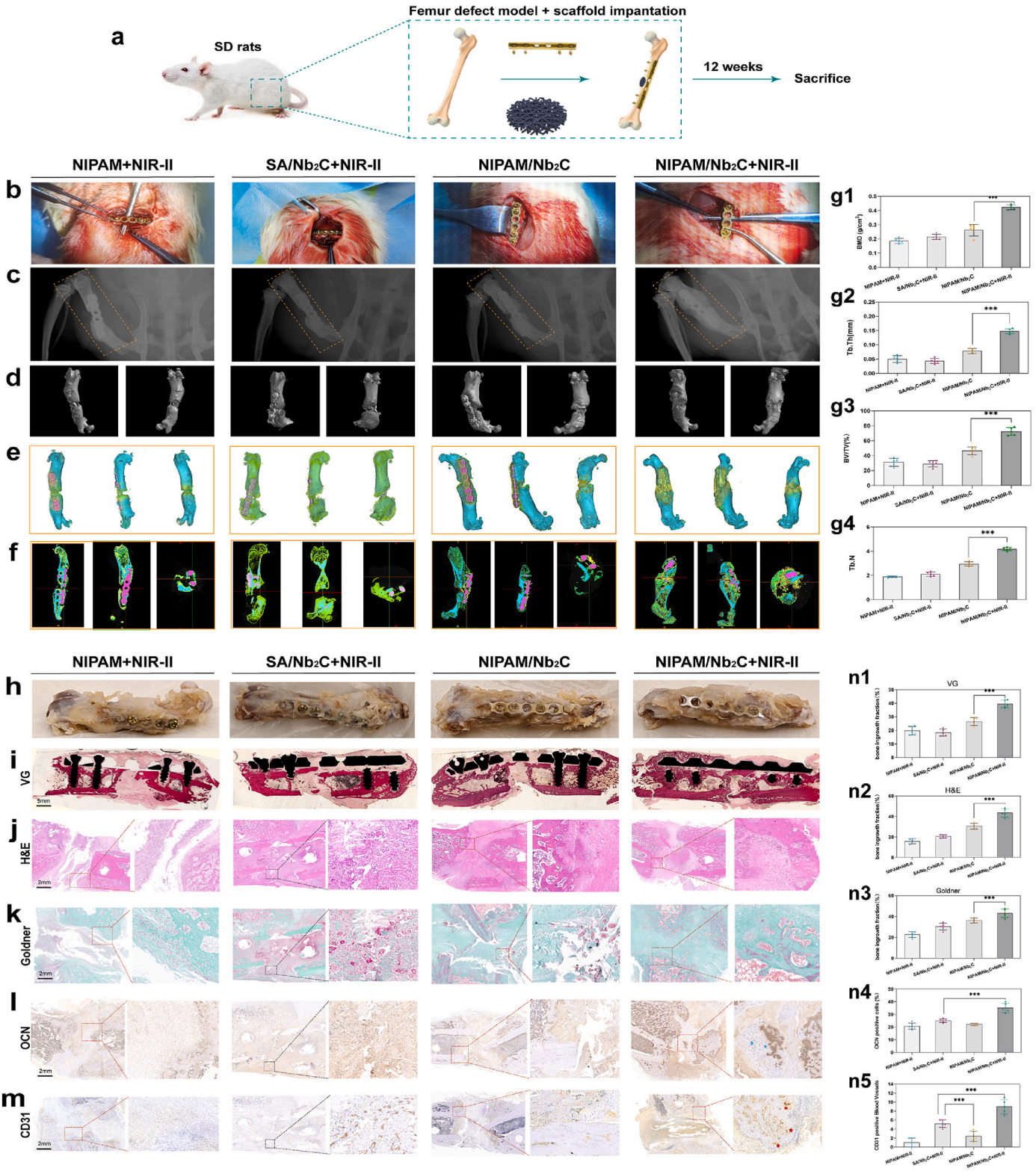

Fig. 5. Micromotion Biomaterial enhanced bone regeneration in femoral shaft defect through the activation of endochondral ossification. a) The *schematic diagram of femoral shaft defect model.* b) Intraoperative photograph of the model of femoral shaft. c) X-ray of femur defect model 12 weeks after implantation of different scaffolds. d) 3D reconstruction of femur defects model. e) 3D reconstruction of new bone (green), osteoid (yellow) and cortical bone (blue). f) Horizontal, sagittal, and coronal planes of the 3D model. g1-g4) Quantitative fundamental parameters of bone mineral density (BMD), trabecular thickness (Tb.Th), bone volume/tissue volume (BV/TV) and trabecular number (Tb.N) in newborn osseous tissue based on the histomorphometric micro-CT analysis. N = 5, *p < 0.05, **p < 0.01, and ***p < 0.001. h) The photograph of femoral shaft 12 weeks after surgery. i) The Van Gieson staining of hard tissue slices of different groups. Scale bar is 5 mm. j-k) The H&E and Goldner staining of femoral shaft in different groups. Scale bar is 2 mm. l) The immunohistochemical staining of OCN in tissue slicing of different groups. The blue stars indicated OCN positive cells. m) The immunohistochemical staining of CD31 in tissue slicing of different groups. The red stars indicated CD31 positive blood vessels. n1-n5) Quantification of bone ingrowth, OCN positive cells and CD31 positive blood vessels based on histochemical staining. N = 5, *p < 0.05, **p < 0.01, and ***p < 0.001.

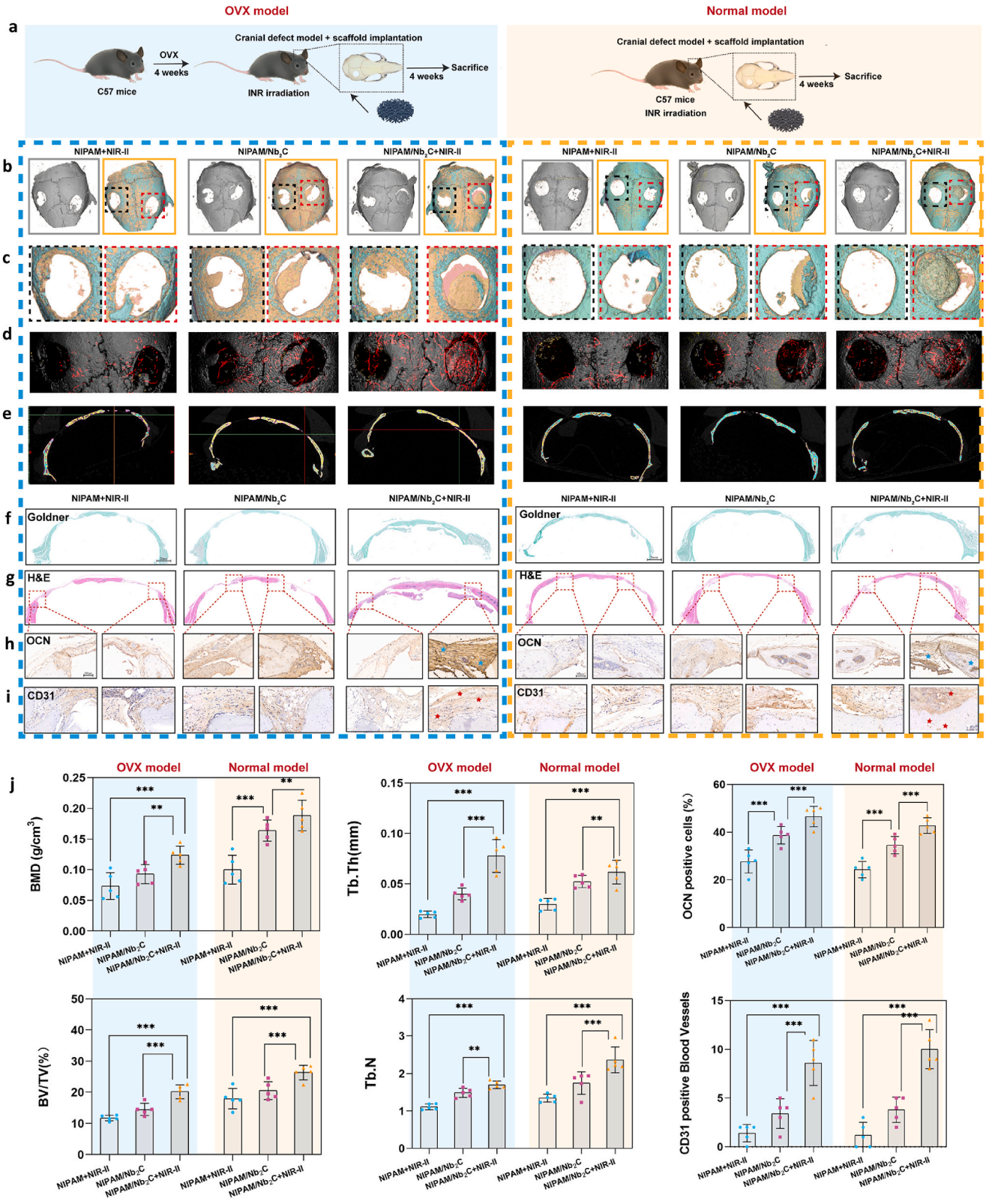

Fig. 6. Micromotion Biomaterial increased bone healing and angiogenesis in calvarial defect model. a) The schematic diagram of calvarial defect model. b) 3D reconstruction of calvarial defects and neovascularization at week 4 after implantation of different scaffolds. c) Magnified images of calvarial defect areas with different color, new bone (pink), osteoid (yellow) and cortical bone (blue). d) Vascular perfusion showed more prominent angiogenesis in NIPAM/Nb_2C + NIR-II groups. e) coronal planes of the 3D model. f,g) The Goldner staining and H&E staining results of different groups. Scale bar is 2 mm. h-i) The immunohistochemical staining of OCN and CD31 of different groups, in OVX mouse model or normal mouse model, respectively. The blue stars indicated OCN positive cells. The red stars indicated CD31 positive blood vessels. Scale bar is 500 μm. j) Quantification of bone mineral density (BMD), trabecular thickness (Tb.Th), bone volume/tissue volume (BV/TV), trabecular number (Tb.N), OCN positive cells and CD31 positive blood vessels in newborn osseous tissue based on the micro-CT analysis and immunohistochemical staining in OVX mouse model or normal mouse model. N = 5, *p < 0.05, **p < 0.01, and ***p < 0.001.

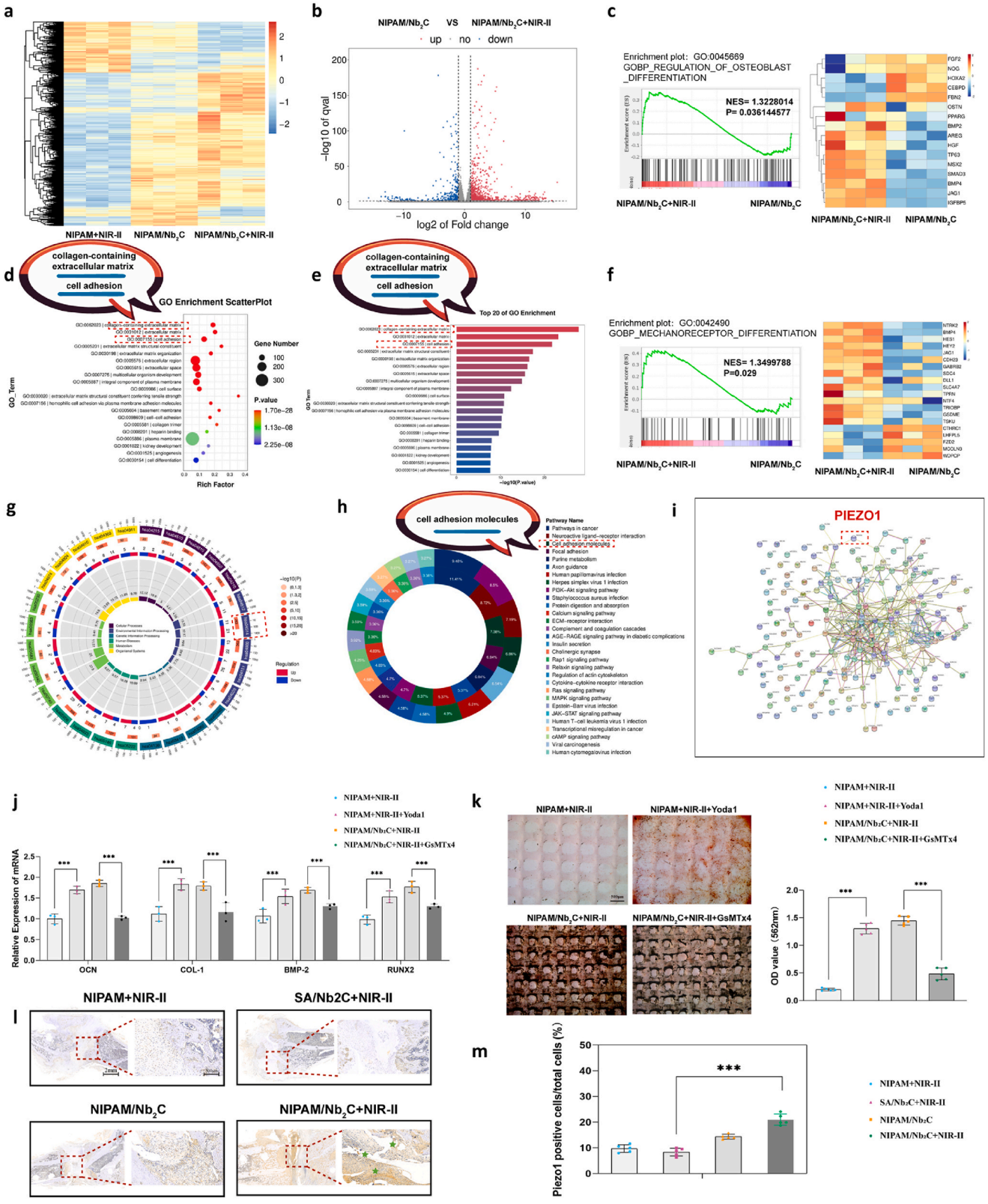

Fig. 7. Micromotion-induced osteogenic differentiation of BMSCs is associated with Piezo1 protein. a) Heatmap of differential gene. b) Volcano map of differential gene. c) Gene set enrichment analysis (GSEA) of osteoblast differentiation related pathways. d) The Gene Ontology (GO) enrichment scatterplot of comparison. e) The top 20 up enrichment GO terms in NIPAM/Nb_2C + NIR-II group. f) GSEA analysis of genes related with mechanoreceptor differentiation pathway. g) The GO enrichment cluster. h) The upregulated or downregulated gene of GO enrichment doughnut. i) The STRING protein interaction network analysis based on the differential genes. j) Osteogenic gene expression (OCN, COL-1, BMP-2, and RUNX2) of BMSCs on day 7 in different groups underwent micromotion and the regulation of Piezo1. k) ARS staining and quantitative statistics of indicated groups. Scale bar is 500 μm. l) The immunohistochemical staining of Piezo1 positive area in femoral shaft defect model. Scale bar is 500 μm. m) Quantification of Piezo1 positive area in. N = 5, *p < 0.05, **p < 0.01, and ***p < 0.001.

conditions for inducing osteogenic differentiation of BMSCs (Fig. 4). In a previous study, a hydrogel with tunable stress relaxation capacity was designed, and strain relaxation was found to be a key modulator of cell fate [84]. BMSCs located within the periosteum, dura mater, and marrow cavity [85,86] serve as osteoprogenitors and facilitate the healing process in either intramembranous ossification (IMO) or ECO [87–89]. Other studies have reported the impact of mechanical cues on cell differentiation, including flow shear stress, topographic changes, and stiffness of the adhesion surface [90–93], most of which suggest that appropriate micromotion could induce BMSCs to differentiate toward the osteogenic lineage. However, the exact optimal magnitude and frequency of micromotion required for the osteogenic differentiation of BMSCs remain unknown. In this study, we found that a cyclic VR alteration of 8.5 % at 1/300 Hz was the most favorable condition for osteogenic differentiation of BMSCs. Furthermore, we discovered that cells displayed peak elongation AR (up to 2.5-fold compared with the control) at 1/350 Hz after 24 h of co-culture, and the highest osteogenic activity at 1/300 Hz (Fig. 4) when co-cultured with the NIPAM/Nb_2C scaffold. These unparalleled results may be attributed to the fact that the osteogenic differentiation of BMSCs is a complicated procedure affected by multiple factors, including VR, frequency, and temperature.

In a living body, cells constantly receive and respond to microenvironmental mechanical cues by deforming themselves [73,74]. Therefore, the destiny and healing modes of bone fractures are variable and non-exclusive. In the present study, we performed implantation surgery in a rat model of femoral shaft defect. According to previous studies, normal bone healing requires a certain amount of axial micromotion at 3 weeks to induce the rapid production of soft calluses [4,14,94]. The most beneficial time point for promoting micromotion was 0–3 weeks [14,94]. First, we found that the micromotion biomaterials significantly facilitated the healing process of femoral shaft defects compared with the control. Second, we found that the volume of soft calluses formed in the early period after fracture was significantly increased by the micromotion stimulus, as well as the number of $MMP13^{(+)}$ hypertrophic chondrocytes. This finding agrees with Perren's theory [95] that a relatively "flexible" microenvironment might favor secondary fracture healing and ECO [96]. A previous study revealed that prolonged micromotion at the fracture site resulted in high interfragmentary strain and repeated destruction of neonatal blood vessels, disrupting the maturation of the ossifying structure and the bone healing process [97,98]. In our study, although the micromotion biomaterials produced an "unstable" microenvironment at the fracture site, the number of $CD31^{(+)}$ nascent blood vessels was increased by the micromotion stimulus at 12 weeks. This may indicate that a mild "flexible" microenvironment significantly promoted the formation and *trans*--differentiation of hypertrophic chondrocytes (the primary generators of VEGF in the fracture healing process), which in turn facilitated nascent blood vessel formation [99–101]. To measure the therapeutic effects of the micromotion biomaterials on defective non-weight-bearing bone, we performed implantation surgery in a calvarial defect model in normal and OVX mice. In addition, these results showed significantly more new bone tissue compared with the control. Taken together, the NIPAM/Nb_2C scaffolds not only exhibited superior biocompatibility but also facilitated the ingrowth of capillaries and full-thickness bone tissue formation along the dura mater at 4 weeks. Natural fracture healing is the most efficient when fine-tuned mechanical force and proper micromotion are applied. Mechanical forces, is indispensable during the process of nature bone healing, including BMSCs differentiation, mineral deposition, and matrix maturation [1,12]. Fine-tuned micromotion is beneficial for the successful bone union and development [9,10]. In animals suffering from bone fractures, the gravity and muscle contractions constantly exert mechanical force on fractured skeletal and result in micromotion, where nonunion rarely occurs. To a certain extent, this Micromotion Biomaterial provides the mechanical force sensed by bone fragments during the natural bone healing process. The development and research of NIPAM/Nb_2C hydrogels indicate that controllable micromotion can facilitate bone callus formation and maturation, which eventually accelerates full-thickness osseous regeneration. This finding might establish a new subclass of biomaterials, Micromotion Biomaterial, capable of providing controllable micromotion among skeletal fragments to mimic the natural healing process of bone fractures.

Through mRNA screening and verification, we found that enhanced osteogenic differentiation of BMSCs induced by micromotion was associated with Piezo1 activation. Previous studies reported that Piezo1 is a key modulator of trabecular formation, osteocyte crosstalk, and BMSC differentiation [102–105]. In our study, using mRNA sequencing and subsequent analyses, we found that focal adhesion pathways were involved (Fig. 7). In a living body, cells constantly receive and respond to microenvironmental mechanical cues by deforming themselves [73,74]. Specifically, in the skeletal system, cells (e.g., MSCs, osteoblasts, and osteocytes) sense and respond to microforces from the local environment and transduce these extracellular signals through a special membrane receptor, Piezo [75,76]. The Piezo1 channel, a member of the Piezo family [77], can convert mechanical cues into biological signals through conformational changes, subsequent clustering of adhesion ligands, and cell skeleton movement [73,76,78]. We found that Piezo1 was significantly upregulated in the NIPAM/Nb_2C + NIR-II group, which was consistent with the ARS results. Downregulation of Piezo1 in co-cultured BMSCs significantly decreased osteogenic differentiation. These data indicate that Piezo1 plays a critical role in the micromotion-mediated osteogenic differentiation of BMSCs.

This study has several limitations. First, we did not observe or measure *in vivo* micromotion at the fracture site. Measurement of the *in vivo* microenvironment is much more complicated than that in an *in vitro* co-culture system. The shear force of blood flow, muscle contraction, and variations in body temperature at the fracture site could lead to fluctuations in the frequency and magnitude of micromotion. Second, in this study, we utilized NIR-II irradiation as an exogenic stimulus to initiate the photothermal conversion process of Nb_2C nanosheets and thus trigger the reversible shrinkage and swelling behavior of the NIPAM/Nb_2C composite hydrogel, namely micromotion. However, NIR-II irradiation suffers from various drawbacks, such as limited penetration depth and undesirable thermal effects on normal tissues. Other exogenic stimuli, such as ultrasound and magnetic resonance, can be explored as better means for the generation of micromotion. Third, it is generally acknowledged that BMSCs are the most important generators of the bone healing process [57,106]; therefore, we focused on cyclic changes in BMSCs *in vitro*. However, bone healing is a sophisticated process, during which a plethora of other cell lineages also play critical roles.

5. Conclusions

In conclusion, this study proposed a novel NIR–II–activated deformable NIPAM/Nb_2C hydrogel by integrating controllable micromotion into a highly biocompatible scaffold that can effectively generate precise micromotion to promote osteogenic differentiation, namely Micromotion Biomaterial. We also validated that micromotion at 1/300 Hz triggered a 2.37-fold change in the cell length/diameter ratio, which is the most favorable condition for the osteogenic differentiation of BMSCs. High-throughput mRNA screening and verification demonstrated that micromotion-enhanced osteogenic differentiation of BMSCs was correlated with the activation of the mechanosensitive channel Piezo1. The mouse calvarial defect model and the rat femoral shaft defect model were established to explore the osteoinductive effect of the NIPAM/Nb_2C composite. *In vivo* results corroborated that controllable micromotion facilitated the natural fracture healing process through the sequential activation of endochondral ossification, promotion of neovascularization, initiation of mineral deposition, and combinatory acceleration of full-thickness osseous regeneration. In summary, we proposed the design of an NIR–II–activated deformable NIPAM/Nb_2C hydrogel scaffold as a Micromotion Biomaterial, which would provide

an intriguing platform for the treatment of massive bone defects and illuminate ideas for the future design of bone regenerative biomaterials.

Ethics approval and consent to participate

All procedures for the care and use of laboratory animals were approved by the Animal Research Committee of Shanghai Sixth People's Hospital Affiliated to Shanghai Jiao Tong University School of Medicine (No. 2022-0006).

Data availability

The datasets generated for this study are available on request from the corresponding authors.

CRediT authorship contribution statement

Qianhao Yang: Writing – review & editing, Writing – original draft, Visualization, Validation, Project administration, Methodology, Investigation, Funding acquisition, Conceptualization. **Mengqiao Xu:** Writing – review & editing, Writing – original draft, Visualization, Formal analysis, Data curation. **Haoyu Fang:** Writing – review & editing, Writing – original draft, Validation, Methodology, Investigation, Funding acquisition, Formal analysis, Data curation. **Youshui Gao:** Writing – review & editing, Methodology, Investigation, Funding acquisition, Formal analysis, Data curation. **Daoyu Zhu:** Writing – review & editing, Methodology, Investigation, Funding acquisition. **Jing Wang:** Writing – review & editing, Validation, Supervision, Methodology, Investigation, Conceptualization. **Yixuan Chen:** Writing – review & editing, Validation, Supervision, Funding acquisition, Conceptualization.

Declaration of competing interest

The authors declare that they have no known competing financial interests or personal relationships that could have appeared to influence the work reported in this paper.

Acknowledgments

This research was funded by the National Natural Science Foundation of China (Grant No. 81902237, 82072417, 82302693); the Shanghai Sailing Program (Grant NO.21YF1433700, 23YF1432400); and the China Postdoctoral Science Foundation (Grant No. 2023M742324). The schematic illustration in Scheme Figure and Graphic Abstract was created with BioRender.com.

Appendix A. Supplementary data

Supplementary data to this article can be found online at https://doi.org/10.1016/j.bioactmat.2024.05.023.

References

[1] E.F. Morgan, R.E. Gleason, L.N. Hayward, P.L. Leong, K.T. Palomares, Mechanotransduction and fracture repair, J. Bone Joint Surg. Am. 90 (Suppl 1) (2008) 25–30, https://doi.org/10.2106/jbjs.G.01164.

[2] S. Stewart, A. Darwood, S. Masouros, C. Higgins, A. Ramasamy, Mechanotransduction in osteogenesis, Bone Jt. Res. 9 (2020) 1–14, https://doi.org/10.1302/2046-3758.91.Bjr-2019-0043.R2.

[3] R. Weinkamer, C. Eberl, P. Fratzl, Mechanoregulation of bone remodeling and healing as inspiration for self-repair in materials, Biomimetics 4 (2019) 46, https://doi.org/10.3390/biomimetics4030046.

[4] T. Einhorn, L. Gerstenfeld, Fracture healing: mechanisms and interventions, Nat. Rev. Rheumatol. 11 (2015) 45–54, https://doi.org/10.1038/nrrheum.2014.164.

[5] S.M. Perren, Fracture healing: fracture healing understood as the result of a fascinating cascade of physical and biological interactions. Part I. An attempt to integrate observations from 30 years AO research, Acta Chir. Orthop. Traumatol. Cechoslov. 81 (2014) 355–364, https://doi.org/10.55095/achot2014/049.

[6] J. Kenwright, J. Richardson, A. Goodship, M. Evans, D. Kelly, A. Spriggins, J. Newman, S. Burrough, J. Harris, D. Rowley, Effect of controlled axial micromovement on healing of tibial fractures, Lancet 2 (1986) 1185–1187, https://doi.org/10.1016/s0140-6736(86)92196-3.

[7] L.E. Claes, C.A. Heigele, C. Neidlinger-Wilke, D. Kaspar, W. Seidl, K. J. Margevicius, P. Augat, Effects of mechanical factors on the fracture healing process, Clin. Orthop. Relat. Res. (1998) S132–S147, https://doi.org/10.1097/00003086-199810001-00015.

[8] J. Glowacki, Angiogenesis in fracture repair, Clin. Orthop. Relat. Res. (1998) S82–S89, https://doi.org/10.1097/00003086-199810001-00010.

[9] S. Herberg, A. McDermott, P. Dang, D. Alt, R. Tang, J. Dawahare, D. Varghai, J. Shin, A. McMillan, A. Dikina, F. He, Y. Lee, Y. Cheng, K. Umemori, P. Wong, H. Park, J. Boerckel, E. Alsberg, Combinatorial morphogenetic and mechanical cues to mimic bone development for defect repair, Sci. Adv. 5 (2019) eaax2476, https://doi.org/10.1126/sciadv.aax2476.

[10] A. McDermott, S. Herberg, D. Mason, J. Collins, H. Pearson, J. Dawahare, R. Tang, A. Patwa, M. Grinstaff, D. Kelly, E. Alsberg, J. Boerckel, Recapitulating bone development through engineered mesenchymal condensations and mechanical cues for tissue regeneration, Sci. Transl. Med. 11 (2019) eaav7756, https://doi.org/10.1126/scitranslmed.aav7756.

[11] C. Dolan, F. Imholt, T. Yang, R. Bokhari, J. Gregory, M. Yan, O. Qureshi, K. Zimmel, K. Sherman, A. Falck, L. Yu, E. Leininger, R. Brunauer, L. Suva, D. Gaddy, L. Dawson, K. Muneoka, Mouse digit tip regeneration is mechanical load-dependent, J. Bone Miner. Res. 37 (2021) 312–322, https://doi.org/10.1002/jbmr.4470.

[12] R.E. Buckeley, C.G. Moran, T. Apivatthakakul, AO Principles of Fracture Management, Thieme Medical Pub, 2018.

[13] V. Glatt, M. Miller, A. Ivkovic, F. Liu, N. Parry, D. Griffin, M. Vrahas, C. Evans, Improved healing of large segmental defects in the rat femur by reverse dynamization in the presence of bone morphogenetic protein-2, J. Bone Joint Surg. Am. 94 (2012) 2063–2073, https://doi.org/10.2106/jbjs.K.01604.

[14] V. Glatt, M. Samchukov, A. Cherkashin, C. Iobst, Reverse dynamization accelerates bone-healing in a large-animal osteotomy model, J. Bone Joint Surg. Am. 103 (2021) 257–263, https://doi.org/10.2106/jbjs.20.00380.

[15] D.R. Carter, G.S. Beaupré, N.J. Giori, J.A. Helms, Mechanobiology of skeletal regeneration, Clin. Orthop. Relat. Res. (1998) S41–S55, https://doi.org/10.1097/00003086-199810001-00006.

[16] P. Kostenuik, F.M. Mirza, Fracture healing physiology and the quest for therapies for delayed healing and nonunion, J. Orthop. Res. 35 (2017) 213–223, https://doi.org/10.1002/jor.23460.

[17] L. Claes, S. Recknagel, A. Ignatius, Fracture healing under healthy and inflammatory conditions, Nat. Rev. Rheumatol. 8 (2012) 133–143, https://doi.org/10.1038/nrrheum.2012.1.

[18] Y. Wei, P. Zhang, R.A. Soomro, Q. Zhu, B. Xu, Advances in the synthesis of 2D MXenes, Adv. Mater. 33 (2021) e2103148, https://doi.org/10.1002/adma.202103148.

[19] L. Li, Q. Cheng, MXene based nanocomposite films, Explorations 2 (2022) 20220049, https://doi.org/10.1002/exp.20220049.

[20] J. Ma, L. Zhang, B. Lei, Multifunctional MXene-based bioactive materials for integrated regeneration therapy, ACS Nano 17 (2023) 19526–19549, https://doi.org/10.1021/acsnano.3c01913.

[21] N.C. Ghosh, S.P. Harimkar, Consolidation and synthesis of MAX phases by spark plasma sintering (SPS): a review. Advances in Science and Technology of Mn+1AXn Phases, Woodhead Publishing, 2012, pp. 47–80.

[22] M.A. Khabisi, F. Shirini, K. Shirini, H. Khorsand, M. Marian, A. Rosenkranz, Additively manufactured MAX- and MXene-composite scaffolds for bone regeneration- recent advances and future perspectives, Colloid Surf. B. Biointerfaces 225 (2023) 113282, https://doi.org/10.1016/j.colsurfb.2023.113282.

[23] Y. Gogotsi, B. Anasori, The rise of MXenes, ACS Nano 13 (2019) 8491–8494, https://doi.org/10.1021/acsnano.9b06394.

[24] D.B. Velusamy, J.K. El-Demellawi, A.M. El-Zohry, A. Giugni, S. Lopatin, M. N. Hedhili, A.E. Mansour, E.D. Fabrizio, O.F. Mohammed, H.N. Alshareef, MXenes for plasmonic photodetection, Adv. Mater. 31 (2019) e1807658, https://doi.org/10.1002/adma.201807658.

[25] Y. Yang, J. Jeon, J.H. Park, M.S. Jeong, B.H. Lee, E. Hwang, S. Lee, Plasmonic transition metal carbide electrodes for high-performance InSe photodetectors, ACS Nano 13 (2019) 8804–8810, https://doi.org/10.1021/acsnano.9b01941.

[26] H. Lin, Y. Wang, S. Gao, Y. Chen, J. Shi, Theranostic 2D tantalum carbide (MXene), Adv. Mater. 30 (2018) 1703284, https://doi.org/10.1002/adma.202003085.

[27] M. Naguib, M. Kurtoglu, V. Presser, J. Lu, J. Niu, M. Heon, L. Hultman, Y. Gogotsi, M.W. Barsoum, Two-dimensional nanocrystals produced by exfoliation of Ti3AlC2, Adv. Mater. 23 (2011) 4248–4253, https://doi.org/10.1002/adma.201102306.

[28] Y. Ibrahim, A. Mohamed, A.M. Abdelgawad, K. Eid, A.M. Abdullah, A. Elzatahry, The recent advances in the mechanical properties of self-standing two-dimensional MXene-based nanostructures: deep insights into the supercapacitor, Nanomaterials 10 (2020) 1916, https://doi.org/10.3390/nano10101916.

[29] F. Quero, A. Rosenkranz, Mechanical performance of binary and ternary hybrid MXene/Nanocellulose hydro- and aerogels – a critical review, Adv. Mater. Interfac. 8 (2021) 2100952, https://doi.org/10.1002/admi.202100952.

[30] P. Sobolciak, A. Ali, M.K. Hassan, M.I. Helal, A. Tanvir, A. Popelka, M.A. Al-Maadeed, I. Krupa, K.A. Mahmoud, 2D Ti3C2Tx (MXene)-reinforced polyvinyl alcohol (PVA) nanofibers with enhanced mechanical and electrical properties, PLoS One 12 (2017) e0183705, https://doi.org/10.1371/journal.pone.0183705.

[31] A. Lipatov, H.D. Lu, M. Alhabeb, B. Anasori, A. Gruverman, Y. Gogotsi, A. Sinitskii, Elastic properties of 2D Ti3C2Tx MXene monolayers and bilayers, Sci. Adv. 4 (2018) eaat0491, https://doi.org/10.1126/sciadv.aat0491.
[32] H. Lin, Y. Chen, J.L. Shi, Insights into 2D MXenes for versatile biomedical applications: current advances and challenges ahead, Adv. Sci. 5 (2018) 1800518, https://doi.org/10.1002/advs.201800518.
[33] N. Driscoll, A.G. Richardson, K. Maleski, B. Anasori, O. Adewole, P. Lelyukh, L. Escobedo, D.K. Cullen, T.H. Lucas, Y. Gogotsi, F. Vitale, Two-dimensional Ti3C2 MXene for high-resolution neural interfaces, ACS Nano 12 (2018) 10419–10429, https://doi.org/10.1021/acsnano.8b06014.
[34] K. Hantanasirisakul, Y. Gogotsi, Electronic and optical properties of 2D transition metal carbides and nitrides (MXenes), Adv. Mater. 30 (2018) e1804779, https://doi.org/10.1002/adma.201804779.
[35] H. Lin, S. Gao, C. Dai, Y. Chen, J. Shi, A two-dimensional biodegradable Niobium Carbide (MXene) for photothermal tumor eradication in NIR-I and NIR-II biowindows, J. Am. Chem. Soc. 139 (2017) 16235–16247, https://doi.org/10.1021/jacs.7b07818.
[36] W. Tang, Z. Dong, R. Zhang, X. Yi, K. Yang, M. Jin, C. Yuan, Z. Xiao, Z. Liu, L. Cheng, Multifunctional two-dimensional core-shell MXene@Gold nanocomposites for enhanced photo-radio combined therapy in the second biological window, ACS Nano 13 (2019) 284–294, https://doi.org/10.1021/acsnano.8b05982.
[37] S. Iravani, R.S. Varma, MXenes and MXene-based materials for tissue engineering and regenerative medicine: recent advances, Mater. Adv. 2 (2021) 2906–2917, https://doi.org/10.1039/d1ma00189b.
[38] G. Perini, A. Rosenkranz, G. Friggeri, D. Zambrano, E. Rosa, A. Augello, V. Palmieri, M. De Spirito, M. Papi, Advanced usage of Ti3C2Tx MXenes for photothermal therapy on different 3D breast cancer models, Biomed. Pharmacother. 153 (2022) 113496, https://doi.org/10.1016/j.biopha.2022.113496.
[39] K. Rasool, M. Helal, A. Ali, C.E. Ren, Y. Gogotsi, K.A. Mahmoud, Antibacterial activity of Ti3C2Tx MXene, ACS Nano 10 (2016) 3674–3684, https://doi.org/10.1021/acsnano.6b00181.
[40] A.A. Shamsabadi, M.S. Gh, B. Anasori, M. Soroush, Antimicrobial mode-of-action of colloidal Ti3C2Tx MXene nanosheets, ACS Sustain. Chem. Eng. 6 (2018) 16586–16596, https://doi.org/10.1021/acssuschemeng.8b03823.
[41] A. Rosenkranz, G. Perini, J.Y. Aguilar-Hurtado, D.F. Zambrano, B. Wang, B. Niccolini, P.C. Henriques, E. Rosa, F. De Maio, G. Delogu, M. De Spirito, V. Palmieri, M. Papi, Laser-mediated antibacterial effects of few- and multi-layer Ti3C2Tx MXenes, Appl. Surf. Sci. 567 (2021) 150795, https://doi.org/10.1016/j.apsusc.2021.150795.
[42] K. Huang, Z. Li, J. Lin, G. Han, P. Huang, Two-dimensional transition metal carbides and nitrides (MXenes) for biomedical applications, Chem. Soc. Rev. 47 (2018) 5109–5124, https://doi.org/10.1039/c7cs00838d.
[43] Q.H. Yang, H.H. Yin, T.M. Xu, D.Y. Zhu, J.H. Yin, Y.X. Chen, X.W. Yu, J.J. Gao, C. Q. Zhang, Y. Chen, Y.S. Gao, Engineering 2D mesoporous silica@MXene-integrated 3D-printing scaffolds for combinatory osteosarcoma therapy and NO-augmented bone regeneration, Small 16 (2020) 1906814, https://doi.org/10.1002/smll.201906814.
[44] J. Huang, Z. Li, Y. Mao, Z. Li, Progress and biomedical applications of MXenes, Nano. Select 2 (2021) 1480–1508, https://doi.org/10.1002/nano.202000309.
[45] W. Lin, M. Kluzek, N. Iuster, E. Shimoni, N. Kampf, R. Goldberg, J. Klein, Cartilage-inspired, lipid-based boundary-lubricated hydrogels, Science 370 (2020) 335–338, https://doi.org/10.1126/science.aay8276.
[46] M. Hua, S. Wu, Y. Ma, Y. Zhao, Z. Chen, I. Frenkel, J. Strzalka, H. Zhou, X. Zhu, X. He, Strong tough hydrogels via the synergy of freeze-casting and salting out, Nature 590 (2021) 594–599, https://doi.org/10.1038/s41586-021-03212-z.
[47] W. Li, X. Yang, P. Lai, L. Shang, Bio-inspired adhesive hydrogel for biomedicine—principles and design strategies, Smart. Med. 1 (2022) e20220024, https://doi.org/10.1002/smmd.20220024.
[48] H. Fang, D. Zhu, Q. Yang, Y. Chen, C. Zhang, J. Gao, Y. Gao, Emerging zero-dimensional to four-dimensional biomaterials for bone regeneration, J. Nanobiotechnol. 20 (2022) 26, https://doi.org/10.1186/s12951-021-01228-1.
[49] S.H. Tan, D.A.C. Chua, J.R.J. Tang, C. Bonnard, D. Leavesley, K. Liang, Design of hydrogel-based scaffolds for in vitro three-dimensional human skin model reconstruction, Acta Biomater. 153 (2022) 13–37, https://doi.org/10.1016/j.actbio.2022.09.068.
[50] C.A. Vilela, C. Correia, A. da Silva Morais, T.C. Santos, A.C. Gertrudes, E. S. Moreira, A.M. Frias, D.A. Learmonth, P. Oliveira, J.M. Oliveira, R.A. Sousa, J. D. Espregueira-Mendes, R.L. Reis, In vitro and in vivo performance of methacrylated gellan gum hydrogel formulations for cartilage repair, J. Biomed. Mater. Res., Part A 106 (2018) 1987–1996, https://doi.org/10.1002/jbm.a.36406.
[51] J.T. Weitkamp, M. Woltje, B. Nusspickel, F.N. Schmidt, D. Aibibu, A. Bayer, D. Eglin, A.R. Armiento, P. Arnold, C. Cherif, R. Lucius, R. Smeets, B. Kurz, P. Behrendt, Silk fiber-reinforced hyaluronic acid-based hydrogel for cartilage tissue engineering, Int. J. Mol. Sci. 22 (2021) 3635, https://doi.org/10.3390/ijms22073635.
[52] F. Lin, Y. Li, W. Cui, Injectable hydrogel microspheres in cartilage repair, Biomed. Technolo. 1 (2023) 18–29, https://doi.org/10.1016/j.bmt.2022.11.002.
[53] H.W. Kang, S.J. Lee, I.K. Ko, C. Kengla, J.J. Yoo, A. Atala, A 3D bioprinting system to produce human-scale tissue constructs with structural integrity, Nat. Biotechnol. 34 (2016) 312–319, https://doi.org/10.1038/nbt.3413.
[54] B. Zhou, X. Jiang, X. Zhou, W. Tan, H. Luo, S. Lei, Y. Yang, GelMA-based bioactive hydrogel scaffolds with multiple bone defect repair functions: therapeutic strategies and recent advances, Biomater. Res. 27 (2023) 86, https://doi.org/10.1186/s40824-023-00422-6.
[55] S.X. Chen, J. Zhang, F. Xue, W. Liu, Y. Kuang, B. Gu, S. Song, H. Chen, In situ forming oxygen/ROS-responsive niche-like hydrogel enabling gelation-triggered chemotherapy and inhibition of metastasis, Bioact. Mater. 21 (2023) 86–96, https://doi.org/10.1016/j.bioactmat.2022.08.002.
[56] Y. Luo, W. Pauer, G.A. Luinstra, Fabrication of thermo-responsive controllable shape-changing hydrogel, Gels 8 (2022) 531, https://doi.org/10.3390/gels8090531.
[57] C. Xie, R. Liang, J. Ye, Z. Peng, H. Sun, Q. Zhu, X. Shen, Y. Hong, H. Wu, W. Sun, X. Yao, J. Li, S. Zhang, X. Zhang, H. Ouyang, High-efficient engineering of osteo-callus organoids for rapid bone regeneration within one month, Biomaterials 288 (2022) 121741, https://doi.org/10.1016/j.biomaterials.2022.121741.
[58] Y.X. Chen, D.Y. Zhu, J. Gao, Z.L. Xu, S.C. Tao, W.J. Yin, Y.L. Zhang, Y.S. Gao, C. Q. Zhang, Diminished membrane recruitment of Akt is instrumental in alcohol-associated osteopenia via the PTEN/Akt/GSK-3beta/beta-catenin axis, FEBS J. 286 (2019) 1101–1119, https://doi.org/10.1111/febs.14754.
[59] X. Yang, H.N.S. Almassri, Q. Zhang, Y. Ma, D. Zhang, M. Chen, X. Wu, Electrosprayed naringin-loaded microsphere/SAIB hybrid depots enhance bone formation in a mouse calvarial defect model, Drug Deliv. 26 (2019) 137–146, https://doi.org/10.1080/10717544.2019.1568620.
[60] S.H.L. Kim, S. Cho, S. Kim, J. Kwon, J. Lee, R.H. Koh, J.H. Park, H. Lee, T.H. Park, N.S. Hwang, Cellular direct conversion by cell penetrable OCT4-30Kc19 protein and BMP4 growth factor, Biomater. Res. 26 (2022) 33, https://doi.org/10.1186/s40824-022-00280-8.
[61] Y. Wang, B. Kong, X. Chen, R. Liu, Y. Zhao, Z. Gu, Q. Jiang, BMSC exosome-enriched acellular fish scale scaffolds promote bone regeneration, J. Nanobiotechnol. 20 (2022) 444, https://doi.org/10.1186/s12951-022-01646-9.
[62] F. Yang, X. Liu, D. Wei, Y. Zhu, F. Wang, X. Liu, F. Yan, X. Zhang, Y. Liu, Topical application of butyl flufenamate ointment promotes cranial defect healing in mice by inducing BMP2 secretion in skin mesenchymal stem cells, Cells 11 (2022) 3620, https://doi.org/10.3390/cells11223620.
[63] M. Bouyer, R. Guillot, J. Lavaud, C. Plettinx, C. Olivier, V. Curry, J. Boutonnat, J. L. Coll, F. Peyrin, V. Josserand, G. Bettega, C. Picart, Surface delivery of tunable doses of BMP-2 from an adaptable polymeric scaffold induces volumetric bone regeneration, Biomaterials 104 (2016) 168–181, https://doi.org/10.1016/j.biomaterials.2016.06.001.
[64] Y.F. Ma, N. Jiang, X. Zhang, C.H. Qin, L. Wang, Y.J. Hu, Q.R. Lin, B. Yu, B. W. Wang, Calcium sulfate induced versus PMMA-induced membrane in a critical-sized femoral defect in a rat model, Sci. Rep. 8 (2018) 637, https://doi.org/10.1038/s41598-017-17430-x.
[65] R.D. Verboket, N. Sohling, M. Heilani, C. Fremdling, A. Schaible, K. Schroder, J. C. Brune, I. Marzi, D. Henrich, The induced membrane technique-the filling matters: evaluation of different forms of membrane filling with and without bone marrow mononuclear cells (BMC) in large femoral bone defects in rats, Biomedicines 10 (2022) 642, https://doi.org/10.3390/biomedicines10030642.
[66] M. Saab, C. Zobrist, N. Blanchemain, B. Martel, F. Chai, Systematic literature review of in vivo rat femoral defect models using biomaterials to improve the induced membrane technique: a comprehensive analysis, EFORT Open. Rev. 9 (2024) 138–145, https://doi.org/10.1530/EOR-23-0055.
[67] Y. Chen, J. Yu, Q. Ke, Y. Gao, C. Zhang, Y. Guo, Bioinspired fabrication of carbonated hydroxyapatite/chitosan nanohybrid scaffolds loaded with TWS119 for bone regeneration, Chem. Eng. J. 341 (2018) 112–125, https://doi.org/10.1016/j.cej.2018.02.010.
[68] J. Wang, Q. Yang, Q. Saiding, L. Chen, M. Liu, Z. Wang, L. Xiang, L. Deng, Y. Chen, W. Cui, Geometric angles and gene expression in cells for structural bone regeneration, Adv. Sci. 10 (2023) e2304111, https://doi.org/10.1002/advs.202304111.
[69] H. Yu, Y. Wang, J. Gao, Y. Gao, C. Zhong, Y. Chen, Application of the neuropeptide NPVF to enhance angiogenesis and osteogenesis in bone regeneration, Commun. Biol. 6 (2023) 197, https://doi.org/10.1038/s42003-023-04567-x.
[70] D. Dempster, J. Compston, M. Drezner, F. Glorieux, J. Kanis, H. Malluche, P. Meunier, S. Ott, R. Recker, A. Parfitt, Standardized nomenclature, symbols, and units for bone histomorphometry: a 2012 update of the report of the ASBMR Histomorphometry Nomenclature Committee, J. Bone Miner. Res. 28 (2013) 2–17, https://doi.org/10.1002/jbmr.1805.
[71] L. Tong, Q. Liao, Y. Zhao, H. Huang, A. Gao, W. Zhang, X. Gao, W. Wei, M. Guan, P.K. Chu, H. Wang, Near-infrared light control of bone regeneration with biodegradable photothermal osteoimplant, Biomaterials 193 (2019) 1–11, https://doi.org/10.1016/j.biomaterials.2018.12.008.
[72] J. Xu, Y. Sun, T. Wu, Y. Liu, L. Shi, J. Zhang, Q. Kang, Y. Chai, G. Li, Enhancement of bone regeneration with the accordion technique via HIF-1α/VEGF activation in a rat distraction osteogenesis model, J. Tissue Eng. Regen. Med. 12 (2018) e1268–e1276, https://doi.org/10.1002/term.2534.
[73] Y.C. Lin, Y.R. Guo, A. Miyagi, J. Levring, R. MacKinnon, S. Scheuring, Force-induced conformational changes in PIEZO1, Nature 573 (2019) 230–234, https://doi.org/10.1038/s41586-019-1499-2.
[74] L. He, G. Si, J. Huang, A.D.T. Samuel, N. Perrimon, Mechanical regulation of stem-cell differentiation by the stretch-activated Piezo channel, Nature 555 (2018) 103–106, https://doi.org/10.1038/nature25744.
[75] A.G. Solis, P. Bielecki, H.R. Steach, L. Sharma, C.C.D. Harman, S. Yun, M.R. de Zoete, J.N. Warnock, S.D.F. To, A.G. York, M. Mack, M.A. Schwartz, C.S. Dela Cruz, N.W. Palm, R. Jackson, R.A. Flavell, Mechanosensation of cyclical force by

PIEZO1 is essential for innate immunity, Nature 573 (2019) 69–74, https://doi.org/10.1038/s41586-019-1485-8.
[76] J. Li, B. Hou, S. Tumova, K. Muraki, A. Bruns, M.J. Ludlow, A. Sedo, A.J. Hyman, L. McKeown, R.S. Young, N.Y. Yuldasheva, Y. Majeed, L.A. Wilson, B. Rode, M. A. Bailey, H.R. Kim, Z. Fu, D.A. Carter, J. Bilton, H. Imrie, P. Ajuh, T.N. Dear, R. M. Cubbon, M.T. Kearney, R.K. Prasad, P.C. Evans, J.F. Ainscough, D.J. Beech, Piezo1 integration of vascular architecture with physiological force, Nature 515 (2014) 279–282, https://doi.org/10.1038/nature13701.
[77] B. Coste, J. Mathur, M. Schmidt, T.J. Earley, S. Ranade, M.J. Petrus, A.E. Dubin, A. Patapoutian, Piezo1 and Piezo2 are essential components of distinct mechanically activated cation channels, Science 330 (2010) 55–60, https://doi.org/10.1126/science.1193270.
[78] J.M. Kefauver, A.B. Ward, A. Patapoutian, Discoveries in structure and physiology of mechanically activated ion channels, Nature 587 (2020) 567–576, https://doi.org/10.1038/s41586-020-2933-1.
[79] A. Hosseini, D.A. Hogg, The effects of paralysis on skeletal development in the chick embryo. I. General effects, J. Anat. 177 (1991) 159–168.
[80] V. Lefebvre, P. Bhattaram, Vertebrate skeletogenesis, Curr. Top. Dev. Biol. 90 (2010) 291–317, https://doi.org/10.1016/s0070-2153(10)90008-2.
[81] Y.X. Chen, R. Zhu, Q.F. Ke, Y.S. Gao, C.Q. Zhang, Y.P. Guo, MgAl layered double hydroxide/chitosan porous scaffolds loaded with PFTα to promote bone regeneration, Nanoscale 9 (2017) 6765–6776, https://doi.org/10.1039/c7nr00601b.
[82] L. Sun, H. Niu, Y. Wu, S. Dong, X. Li, B.Y.S. Kim, C. Liu, Y. Ma, W. Jiang, Y. Yuan, Bio-integrated scaffold facilitates large bone regeneration dominated by endochondral ossification, Bioact. Mater. 35 (2024) 208–227, https://doi.org/10.1016/j.bioactmat.2024.01.019.
[83] H. Wu, H. Dong, Z. Tang, Y. Chen, Y. Liu, M. Wang, X. Wei, N. Wang, S. Bao, D. Yu, Z. Wu, Z. Yang, X. Li, Z. Guo, L. Shi, Electrical stimulation of piezoelectric BaTiO3 coated Ti6Al4V scaffolds promotes anti-inflammatory polarization of macrophages and bone repair via MAPK/JNK inhibition and OXPHOS activation, Biomaterials 293 (2023) 121990, https://doi.org/10.1016/j.biomaterials.2022.121990.
[84] O. Chaudhuri, L. Gu, D. Klumpers, M. Darnell, S.A. Bencherif, J.C. Weaver, N. Huebsch, H.P. Lee, E. Lippens, G.N. Duda, D.J. Mooney, Hydrogels with tunable stress relaxation regulate stem cell fate and activity, Nat. Mater. 15 (2016) 326–334, https://doi.org/10.1038/nmat4489.
[85] B. Levi, E.R. Nelson, S. Li, A.W. James, J.S. Hyun, D.T. Montoro, M. Lee, J. P. Glotzbach, G.W. Commons, M.T. Longaker, Dura mater stimulates human adipose-derived stromal cells to undergo bone formation in mouse calvarial defects, Stem Cell. 29 (2011) 1241–1255, https://doi.org/10.1002/stem.670.
[86] M. Pranskunas, E. Šimoliūnas, M. Alksne, V. Martin, P.S. Gomes, A. Puisys, A. Kaupinis, G. Juodzbalys, Assessment of the bone healing process mediated by periosteum-derived mesenchymal stem cells' secretome and a xenogenic bioceramic-an in vivo study in the rabbit critical size calvarial defect model, Materials 14 (2021) 3512, https://doi.org/10.3390/ma14133512.
[87] S.F. Carroll, C.T. Buckley, D.J. Kelly, Cyclic tensile strain can play a role in directing both intramembranous and endochondral ossification of mesenchymal stem cells, Front. Bioeng. Biotechnol. 5 (2017) 73, https://doi.org/10.3389/fbioe.2017.00073.
[88] J. van der Stok, M.K. Koolen, H. Jahr, N. Kops, J.H. Waarsing, H. Weinans, O. P. van der Jagt, Chondrogenically differentiated mesenchymal stromal cell pellets stimulate endochondral bone regeneration in critical-sized bone defects, Eur. Cells Mater. 27 (2014) 137–148, https://doi.org/10.22203/ecm.v027a11.
[89] S. Brielle, D. Bavli, A. Motzik, Y. Kan-Tor, X. Sun, C. Kozulin, B. Avni, O. Ram, A. Buxboim, Delineating the heterogeneity of matrix-directed differentiation toward soft and stiff tissue lineages via single-cell profiling, Proc. Natl. Acad. Sci. U. S. A 118 (2021) e2016322118, https://doi.org/10.1073/pnas.2016322118.
[90] W. Zhang, G. Chu, H. Wang, S. Chen, B. Li, F. Han, Effects of matrix stiffness on the differentiation of multipotent stem cells, Curr. Stem Cell Res. Ther. 15 (2020) 449–461, https://doi.org/10.2174/1574888x15666200408114632.
[91] G. Chen, Y. Lv, P. Guo, C. Lin, X. Zhang, L. Yang, Z. Xu, Matrix mechanics and fluid shear stress control stem cells fate in three dimensional microenvironment, Curr. Stem Cell Res. Ther. 8 (2013) 313–323, https://doi.org/10.2174/1574888x11308040007.
[92] A. Isomursu, M. Lerche, M.E. Taskinen, J. Ivaska, E. Peuhu, Integrin signaling and mechanotransduction in regulation of somatic stem cells, Exp. Cell Res. 378 (2019) 217–225, https://doi.org/10.1016/j.yexcr.2019.01.027.
[93] A.E. Stanton, X. Tong, F. Yang, Extracellular matrix type modulates mechanotransduction of stem cells, Acta Biomater. 96 (2019) 310–320, https://doi.org/10.1016/j.actbio.2019.06.048.
[94] V. Glatt, S. Tepic, C. Evans, Reverse dynamization: a novel approach to bone healing, J. Am. Acad. Orthop. Surg. 24 (2016) e60–e61, https://doi.org/10.5435/jaaos-d-16-00239.
[95] R.W. Hente, S.M. Perren, Tissue deformation controlling fracture healing, J. Biomech. 125 (2021) 110576, https://doi.org/10.1016/j.jbiomech.2021.110576.
[96] H.K. Uhthoff, Current concepts of internal fixation of fractures, Can. J. Surg. 23 (1980) 213–214.
[97] D.R. Carter, P.R. Blenman, G.S. Beaupré, Correlations between mechanical stress history and tissue differentiation in initial fracture healing, J. Orthop. Res. 6 (1988) 736–748, https://doi.org/10.1002/jor.1100060517.
[98] L. Claes, P. Augat, G. Suger, H.J. Wilke, Influence of size and stability of the osteotomy gap on the success of fracture healing, J. Orthop. Res. 15 (1997) 577–584, https://doi.org/10.1002/jor.1100150414.
[99] S. Stegen, G. Carmeliet, The skeletal vascular system - breathing life into bone tissue, Bone 115 (2018) 50–58, https://doi.org/10.1016/j.bone.2017.08.022.
[100] S.A. Hallett, W. Ono, N. Ono, The hypertrophic chondrocyte: to be or not to be, Histol. Histopathology (Oxf.) 36 (2021) 1021–1036, https://doi.org/10.14670/hh-18-355.
[101] D.P. Hu, F. Ferro, F. Yang, A.J. Taylor, W. Chang, T. Miclau, R.S. Marcucio, C. S. Bahney, Cartilage to bone transformation during fracture healing is coordinated by the invading vasculature and induction of the core pluripotency genes, Development 144 (2017) 221–234, https://doi.org/10.1242/dev.130807.
[102] G. Hendrickx, V. Fischer, A. Liedert, S. von Kroge, M. Haffner-Luntzer, L. Brylka, E. Pawlus, M. Schweizer, T. Yorgan, A. Baranowsky, T. Rolvien, M. Neven, U. Schumacher, D.J. Beech, M. Amling, A. Ignatius, T. Schinke, Piezo1 inactivation in chondrocytes impairs trabecular bone formation, J. Bone Miner. Res. 36 (2021) 369–384, https://doi.org/10.1002/jbmr.4198.
[103] X. Xu, S. Liu, H. Liu, K. Ru, Y. Jia, Z. Wu, S. Liang, Z. Khan, Z. Chen, A. Qian, L. Hu, Piezo channels: awesome mechanosensitive structures in cellular mechanotransduction and their role in bone, Int. J. Mol. Sci. 22 (2021) 6429, https://doi.org/10.3390/ijms22126429.
[104] A. Sugimoto, A. Miyazaki, K. Kawarabayashi, M. Shono, Y. Akazawa, T. Hasegawa, K. Ueda-Yamaguchi, T. Kitamura, K. Yoshizaki, S. Fukumoto, T. Iwamoto, Piezo type mechanosensitive ion channel component 1 functions as a regulator of the cell fate determination of mesenchymal stem cells, Sci. Rep. 7 (2017) 17696, https://doi.org/10.1038/s41598-017-18089-0.
[105] L. Wang, X. You, S. Lotinun, L. Zhang, N. Wu, W. Zou, Mechanical sensing protein PIEZO1 regulates bone homeostasis via osteoblast-osteoclast crosstalk, Nat. Commun. 11 (2020) 282, https://doi.org/10.1038/s41467-019-14146-6.
[106] B. Cai, D. Lin, Y. Li, L. Wang, J. Xie, T. Dai, F. Liu, M. Tang, L. Tian, Y. Yuan, L. Kong, S. Shen, N2-polarized neutrophils guide bone mesenchymal stem cell recruitment and initiate bone regeneration: a missing piece of the bone regeneration puzzle, Adv. Sci. 8 (2021) e2100584, https://doi.org/10.1002/advs.202100584.